PHYSICAL REVIEW A VOLUME 38, NUMBER 5 SEPTEMBER 1, 1988

Laser optogalvanic and fluorescence studies of the cathode region of a glow discharge

E. A. Den Hartog, D. A. Doughty, and J. E. Lawler
Department of Physics, University of Wisconsin, Madison, Wisconsin 53706

(Received 15 December 1987; revised manuscript received 4 April 1988)

Various laser diagnostics are used to study the cathode-fall and negative-glow regions of a He glow discharge with a cold Al cathode. The electric field and absolute metastable densities are mapped and the gas temperature is measured over a range of current densities from a near-normal (173 V) to a highly abnormal (600 V) cathode fall. These measurements are analyzed to yield the current balance at the cathode surface, the ionization rate in the cathode-fall region, and the metastable production rate in the cathode-fall and negative-glow regions. The experimental results compare favorably with the results of Monte Carlo simulations. The density and temperature of the low-energy electron gas in the negative glow is determined by combining information from the experiments and Monte Carlo simulations.

I. INTRODUCTION

There has in recent years been a very substantial effort toward the development of a quantitative microscopic understanding of the cathode region of glow discharges.[1-6] This region is of great practical interest because of its importance in plasma processing and in pulsed power devices. Plasma processing includes applications of glow discharges in ion etching, thin-film deposition, and plasma treating of surfaces. The stability of pulsed gas discharge lasers and other pulsed power devices is largely determined by the stability of the cathode-fall region.

The cathode region is also of great fundamental interest. The hydrodynamic approximation, which is often very useful in the central region of a discharge, fails in the cathode region. If the local E/N (electric field to gas density ratio) determines the velocity dependence of the electron distribution function, then the electrons are in hydrodynamic equilibrium.[7] The lack of hydrodynamic equilibrium in the cathode-fall region is caused by the large and rapidly changing E/N, and by the proximity of the electrode. The cathode region includes both the cathode-fall and negative-glow regions. The negative glow has a high density of low-energy electrons and very small electric fields. It also is a nonhydrodynamic region because of a low density of high-energy "beam" electrons injected from the cathode-fall region. Unfortunately the extensive data base of electron transport coefficients such as drift velocities, diffusion coefficients, and Townsend coefficients is not directly applicable in modeling the cathode region.[8] These coefficients are generally measured in drift tube experiments in which considerable effort is devoted to ensuring that the hydrodynamic approximation holds.

Nonequilibrium regions are receiving increased attention from theorist and experimentalist.[9-12] Because of their nonequilibrium nature, electrons in the cathode-fall region are often modeled using either a full Boltzmann equation analysis or a Monte Carlo simulation. A somewhat less realistic but much faster approach is based on a model distribution function with position-dependent parameters.[13] The spatial dependences of the parameters such as electron density, average velocity, and average energy, are determined by solving moments of the Boltzmann equation which are coupled ordinary differential equations. These approaches might in general be called nonequilibrium fluid models. Single-beam and multiple-beam models are examples of this general approach.[14,15] This approach is attractive because it is usually easier and faster to solve moments of the Boltzmann equation which are coupled ordinary differential equations than it is to solve the full Boltzmann equation which is a partial differentio-integral equation. The nonequilibrium fluid approach can in principle be made quite realistic if one is sufficiently clever in the design of a model distribution function for the electrons.

A more complete solution will require a calculation of self-consistent space-charge electric fields. This will involve coupling Poisson's equation and one (or more) moment equation(s) for ions to the moment equations for electrons. Consider a model which includes three moments of the Boltzmann equation for electrons, Poisson's equation, and a single continuity equation for ions. This model requires the simultaneous solution of five coupled first-order differential equations. Four natural boundary conditions include specifying the electron distribution function at the cathode and specifying an electron emission coefficient for ion bombardment of the cathode. The "missing" condition is unfortunately not a boundary condition but rather an extremum condition. The physically correct solution will maximize the current at fixed voltage or minimize the voltage at fixed current.

The problem described in the preceding paragraph is obviously quite difficult. It is also incomplete because of the important role played by metastable atoms, and uv or vacuum ultraviolet (vuv) photons in releasing electrons from the cathode. Appropriate balance equations for these neutral particles must also be included in the problem.

A complete solution to the cathode-fall problem is beyond the scope of this paper. This paper describes extensive experimental results from recently developed laser optogalvanic diagnostics, and more traditional laser-induced fluorescence and laser absorption diagnostics.[16] These experimental results include electric field maps, gas temperature (density) measurements, and absolute metastable density maps in a He glow discharge over a range of current densities from a near-normal cathode fall of 173 V to a highly abnormal cathode fall of 600 V. These experimental results are analyzed in detail to provide information on electron-impact ionization and excitation in the cathode-fall and negative-glow regions. Monte Carlo simulations of electron avalanches in the cathode region are compared to the experimental results. The Monte Carlo code is based on the Boeuf-Marode variation of the null collision technique for nonuniform fields.[17] The agreement of the Monte Carlo results and the experimentally derived ionization and excitation rates is generally good. Finally, the experimental results are combined with Monte Carlo simulations to infer the density and temperature of the low-energy electron gas in the negative glow. This unexpected information is largely based on observation of a suppression of the $2\,^1S$ metastable density in the negative glow due to metastable spin conversion by low-energy electron collisions.

The results of this paper can be viewed in several ways: (1) as a test of our understanding of the key physical processes in the cathode region, (2) as a set of benchmark experiments for further modeling of the cathode region, or (3) as a starting point for more ambitious experiments to study electron emission from the cathode. We plan to make *in situ* determinations of the relative importance of, and coefficients for, electron emission due to ion, metastable atom, and uv or vuv photon bombardment of the cathode.

The structure of this paper is as follows. Section II is a description of the experimental apparatus. Sections III and IV are, respectively, a presentation of the electric field and gas density measurements, and an analysis of this data to yield information on ionization in the cathode-fall region. The field maps and gas density measurements are combined with an analytic treatment of ion transport in the cathode-fall region to determine the current balance, or ratio of ion to electron current at the surface of the cathode. This ratio is found to be 3.3 and is independent of the total discharge current. Sections V and VI are respectively, a presentation of the metastable density maps and an analysis of metastable diffusion and kinetics in the cathode-fall and negative-glow regions. The analysis of the data yields $2\,^1S$ and $2\,^3S$ metastable production rates and a rate for $2\,^1S$ metastable quenching due to low-energy electron collisions in the negative glow. Sections VII and VIII are, respectively, a discussion of the Monte Carlo code including electron-impact cross sections and a comparison of the Monte Carlo results with the experimental results. Section IX is an analysis of the density and temperature of the low-energy electrons in the negative glow. Finally, Sec. X includes a summary, some conclusions, as well as speculations on future work.

II. EXPERIMENTAL APPARATUS

Figure 1 is a schematic of the experimental apparatus. The discharge used in these studies is produced between

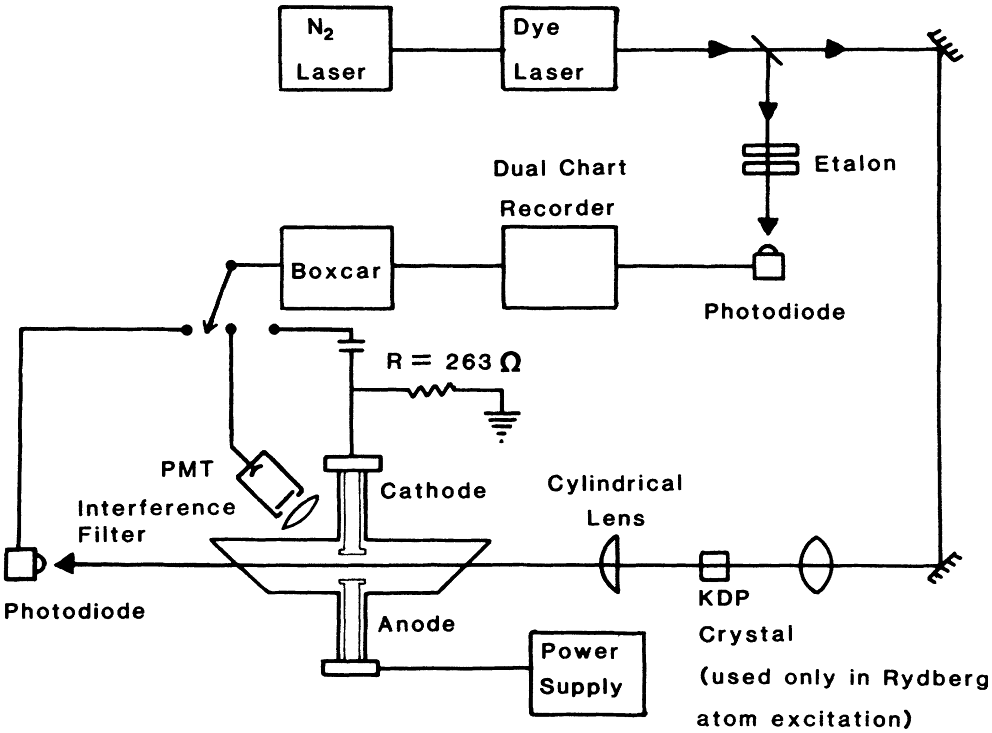

FIG. 1. Schematic of the experimental apparatus showing all three detection methods: optogalvanic, fluorescence, and absorption detection.

flat circular Al electrodes 3.2 cm in diameter and separated by 0.62 cm. The electrodes are water cooled to minimize gas heating. The discharge tube is made primarily of glass and stainless steel. Most of the large seals are made with knife edge flanges on Cu gaskets. The only exceptions are the high-vacuum epoxy seals around the fused silica brewster windows. A liquid-N_2 trapped diffusion pump evacuates the tube to 2×10^{-8} Torr. When no liquid N_2 is in the trap an ion pump maintains the vacuum to prevent oil from backdiffusing into the system. The leak rate into the sealed discharge tube is approximately 3×10^{-4} Torr/day. For discharge operation ultrahigh-purity (0.999 999) He is slowly flowed through the system. A capacitive manometer monitors the pressure which is maintained at 3.5 Torr. The He first passes through a cataphoresis discharge to remove any residual contaminants before entering the main discharge tube. Emission spectra reveal only weak Al and H impurity lines. Although He is much less effective at sputtering than heavy inert gases, some sputtering of the Al cathode does occur. We suspect that the slow erosion of the cathode gives rise to both the weak Al and H impurity lines. Many metals absorb hydrogen. The surface of the Al cathode is cleaned *in situ* by running an Ar discharge. Argon is very effective at sputtering most metals including Al. A carefully prepared cathode provides discharge *V-I* characteristics which are stable to a few percent over a period of a month.

Experiments are carried out over a range of discharge current densities from 0.190 to 1.50 mA/cm^2. The low current density corresponds to a near-normal cathode-fall voltage of 173 V and the high current density corresponds to a highly abnormal cathode-fall voltage of 600 V. The discharge current is spread uniformly across the surface of the electrodes. The absence of significant fringing was verified by segmenting the 3.2-cm-diam cathode into a 1.6-cm-diam disk and a close-fitting annulus with an outside diameter of 3.2 cm. Each part of the cathode was maintained at the same potential during operation and the average current density on each was measured. The current density was found to be uniform across the cathode. This measurement is one of the justifications for using one-dimensional models of the cathode-fall region. The segmented cathode was replaced by a solid cathode after the current-density measurements.

The laser used is a N_2 laser pumped dye laser. Several different configurations for the dye laser are used, depending on the specific experiment. The dye laser bandwidth is 0.3 cm^{-1} without an ètalon. An ètalon is used to reduce the bandwidth to 0.01 cm^{-1} (300 MHz) for some measurements. The dye laser with frequency doubling is tunable over a wavelength range 200–700 nm.

Figure 1 shows all three detection schemes used in these experiments. Optogalvanic detection, fluorescence detection, and absorption detection each has unique advantages which are discussed in subsequent sections. In order to perform spatially resolved measurements without disturbing laser alignment the discharge is mounted on a precision translation stage. Good spatial resolution is achieved, when necessary, by passing the laser beam through a narrow slit and imaging the slit into the discharge region.

III. ELECTRIC FIELD AND GAS DENSITY MEASUREMENTS

Space-charge electric fields in gas discharges have traditionally been measured using electron beam deflection. A laser-induced fluorescence technique for field measurements was recently developed by Moore, Davis, and Gottscho.[18] A laser technique based on optogalvanic detection of Rydberg atoms was recently developed by Doughty, Salih, and Lawler.[16,19] Both laser techniques have a number of important advantages over the traditional electron beam deflection technique.[20] The laser techniques are useful at higher pressures and discharge current densities. It is easier to use a spectroscopic technique in a high-purity discharge system. The laser techniques are truly nonperturbing when performed with a nanosecond pulsed laser because the field is measured when the atoms or molecules absorb the laser light, and any perturbation to the discharge fields occurs on a longer-time scale. Lasers have the potential for making measurements with a few microns spatial resolution and nanosecond temporal resolution. The technique based on Rydberg atoms has broad applicability because all atoms and molecules have Rydberg levels. This technique also has a wide dynamic range because one can choose an appropriate principal quantum number. The Rydberg atom technique has been used to measure fields as small as 10±1 V/cm.[21]

The technique based on optogalvanic detection of Rydberg atoms excited with a single laser is used in this investigation.[16] A technique involving intersecting laser beams for pinpoint field measurements has also been demonstrated.[19] The discharge studied in this experiment is sufficiently one dimensional that the simpler single laser technique is adequate. In addition to the advantages described in the preceding paragraph, a Rydberg atom technique offers an advantage in ease of interpretation. The experimental Stark spectra are analyzed by comparing to theoretical Stark maps. Straightforward, *ab initio* calculations of these Stark maps to 1% accuracy are possible for many atoms. An excellent procedure for calculating the Stark maps is described in detail by Zimmerman, Littman, Kash, and Kleppner.[22] The procedure used in this work is a simplified version of that described by Zimmerman *et al.* The main simplification is that we use corrected hydrogenic radial matrix elements instead of performing a numerical integration for radial matrix elements.

A Rydberg atom is an atom with one of its electrons excited to a high-lying energy level characterized by a large principal quantum number *n*. As *n* increases, many atomic properties tend towards those of hydrogen. The energy of Rydberg states is given by the empirical formula,

$$W_{nl}=W_{\text{ion}}-\frac{R_0}{(n-\delta_l)^2}\ , \tag{1}$$

where W_{ion} is the ionization potential, R_0 is the Rydberg constant, l is the angular momentum quantum number, and δ_l is the quantum defect. This expression describes hydrogenic energy levels for $\delta_l = 0$. The quantum defect reflects the degree of interaction of the outer valence electron with the core electrons.

Mixing of states with different principal quantum numbers occurs if both the field and principal quantum number are sufficiently large. This is an undesirable complication if one is studying a discharge and simply using Rydberg atoms as a probe. It can usually be avoided by choosing an appropriate, somewhat lower principal number for very high fields. In heavy atoms with large quantum defects it may be necessary to include states, which are nearby at zero field, but have different principal quantum numbers. In He all quantum defects are less than 0.5.

The energy perturbations are calculated by diagonalizing an $(n-m)$ by $(n-m)$ Hamiltonian matrix, where m is the component of angular momentum along the field axis. The basis set is made of eigenfunctions of the unperturbed Hamiltonian. The diagonal matrix elements are the unperturbed energies of the levels as given in Eq. (1). The quantum defect δ_l can be deduced from Moore's tables of energy levels.[23] The off-diagonal elements vanish except those connecting states for which l differs by 1. These matrix elements are approximately the hydrogenic matrix elements given by the expression

$$\langle n\ l\ m \,|\, e\mathbf{E}\cdot\mathbf{r} \,|\, n\ l-1\ m \rangle = (\tfrac{3}{2}) eEa_0 n \left[\frac{(n^2-l^2)(l^2-m^2)}{4l^2-1} \right]^{1/2} . \quad (2)$$

where e is the unit charge and a_0 is the Bohr radius. The dipole matrix elements above must be corrected to account for core penetration effects. A correction factor of order 1 has been tabulated as a function of quantum defect by Edmonds *et al.*[24]

Figure 2 presents the results of applying the procedure outlined above to the $n=11$, $m=0$, singlet levels of He. The diagonal elements are determined from the splittings of the $11\,^1S$, $11\,^1P$, $11\,^1D$, $11\,^1F$, and $11\,^1G$ levels, whereas the *H*, *I*, *K*, *L*, *M*, and *N* levels are approximated as being degenerate with the $11\,^1G$ level.[23] A 5% correction is applied to the *S*-*P* matrix elements to account for core penetration.[24] Corrections to the other elements are generally less than 1%. Figure 2(a) is a plot of the energies of the $m=0$ states for the $n=11$ levels as a function of applied electric field. The energies are the eigenvalues of the diagonalized Hamiltonian. Only ten components appear in this figure since the $11\,^1S$ level has a large quantum defect and is 23 cm^{-1} below this pattern. This level does not mix strongly with the other $n=11$ levels at the fields indicated in the figure. For fields above 200 V/cm the pattern clearly reflects a linear Stark effect.

Figure 2(b) is a plot of the expected intensity of selected Stark components from Fig. 2(a) as a function of electric field. Suppose transitions between a low-lying non-Rydberg ^1S level and the $n=11$ Rydberg states are driven. With no external electric field, only the $^1S \rightarrow 11\,^1P$ transition will be observed. The effect of the field is to mix a fraction of the $11\,^1P$ state into each $n=11$ state. This fraction is determined by squaring the appropriate element from an eigenvector of the diagonalized Hamiltonian. The fraction is a relative linestrength for a transition to that component of the Stark manifold. The relative linestrengths of the components labeled 1, 3, and 8 are plotted in Fig. 2(b). Such information is useful

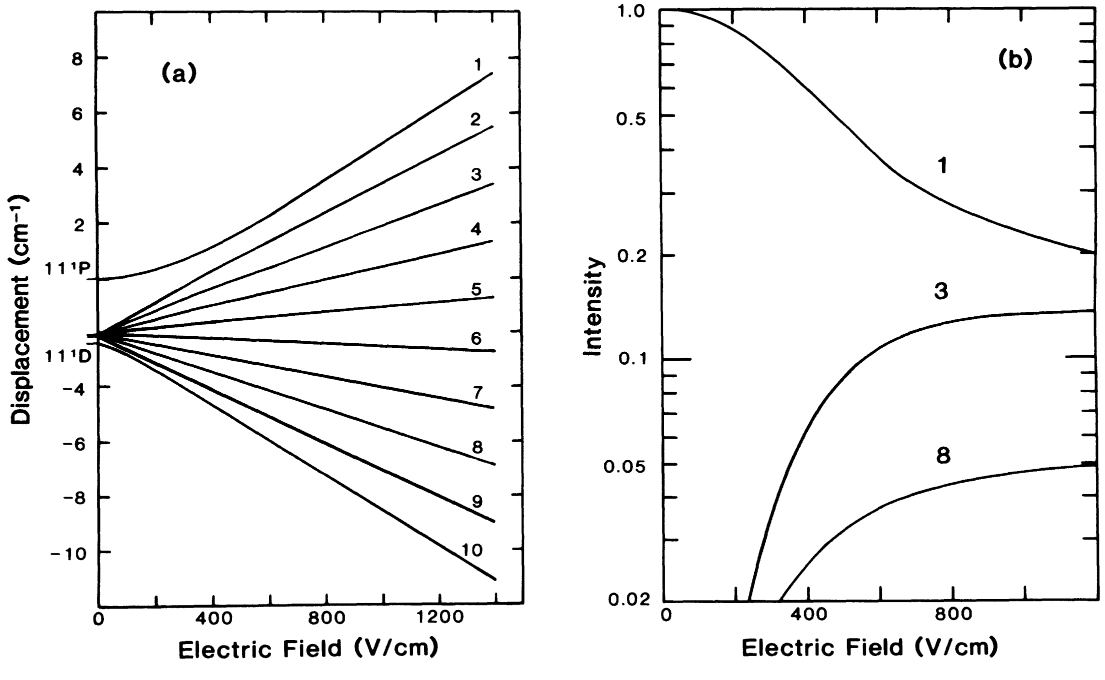

FIG. 2. (a) Theoretical Stark map for the $n=11$ singlet $m=0$ levels of He. (b) Theoretical intensities of selected Stark components as a function of electric field.

in determining electric fields in the case where the splittings between individual components are small.

The narrow bandwidth, high power dye laser is ideal for exciting atoms from a well-populated lower level to a specific Rydberg level. Since the oscillator strength decreases as $1/n^3$ it is very difficult to directly detect the weak absorption. Laser-induced fluorescence from these atoms is also difficult to detect, because in the 1–10 Torr pressure regime the Rydberg atoms do not survive long enough to radiate. They are collisionally ionized via collisions with ground-state atoms. Associative ionization,

$$\mathrm{He}^*(nl>3s)+\mathrm{He}(1\,^1S_0)\rightarrow \mathrm{He}_2{}^+ + e^- \ , \tag{3}$$

is likely important for Rydberg levels below the ionization limit by more than thermal energies. The absorption of laser radiation produces excess ionization in the discharge and thus produces an optogalvanic effect. An optogalvanic effect is detectable as a perturbation of the discharge current and can in general be either positive (increased current) or negative. Absorption of radiation may in some cases cause a reduction of ionization in the discharge and a decrease in discharge current.[25] Optogalvanic spectroscopy is uniquely suited to the detection of Rydberg atoms in a discharge environment.

The cathode-fall region is particularly well suited to optogalvanic detection. If an extra ion-electron pair is introduced into the cathode-fall region the electron is accelerated by the field, thus producing additional ionization. This amplification can result in optogalvanic effects in the cathode-fall region that are 100 times more sensitive than optogalvanic effects in the positive column.[26]

If the lower level from which the transition is driven is metastable, the ionization process results in the destruction of the metastable atom. The destruction of atoms in these levels can produce a negative optogalvanic effect since metastables diffusing to the cathode have a large probability of releasing electrons from the cathode. It would seem that this negative optogalvanic effect might cancel the positive optogalvanic effect which is due to the extra electron produced by associative ionization. The time scales for the two signals, however, are vastly different. The diffusion time of the metastables to the cathode can be several hundred microseconds, whereas associative ionization produces a signal in less than 1 μsec. When produced by a pulsed laser the positive portion of the transient optogalvanic signal is well isolated and can be easily monitored with a boxcar averager.

The critical consideration in measuring discharge electric fields is choosing an appropriate transition to produce the Rydberg atoms. For noble gases in general and He in particular, transitions from the ground state to upper levels are inaccessible with present dye lasers. These gases, however, have metastable levels which are well populated in the discharge. In He, both $2\,^1S$ and $2\,^3S$ levels are metastable. The $2\,^1S$ to $11\,^1P$ transition at 321 nm is the most suitable under the conditions of this experiment. Although the $2\,^3S$ level has a higher population than the $2\,^1S$, the $n\,^3P$ levels have a much higher quantum defect than the $n\,^1P$'s (0.068 and -0.012, respectively).[23] The larger quantum defect necessitates exciting to a level with a larger n to observe a linear Stark effect for a given field. The oscillator strength goes as $1/n^3$ while the number of components increases as n, so the amount of signal in each component drops as $1/n^4$.

Radiation from the dye laser is frequency doubled using a potassium dihydrogen phosphate crystal. The frequency doubled beam is polarized normal to the surface of the cathode so that only $\Delta m=0$ transitions are excited. This results in only $m=0$ Rydberg states because the lower level is a ^1S. The beam is focused in the center of the discharge to a strip approximately 0.01 cm wide and 1 cm long parallel to the surface of the electrodes. As the laser is scanned through the Stark manifold, the current is monitored across a 263 Ω resistor between the cathode and ground. The optogalvanic signal is processed using a boxcar averager, the output of which is plotted on one channel of a two-channel chart recorder. Figure 3 includes representative Stark spectra for a range of distances from the cathode. The splittings of adjacent components or the width of the entire Stark manifold are compared to the Stark map of Fig. 2(a) to determine the local electric field. A relative frequency calibration is obtained by use of an étalon with an accurately determined spacer. Interference fringes are generated and recorded simultaneously with the spectrum.

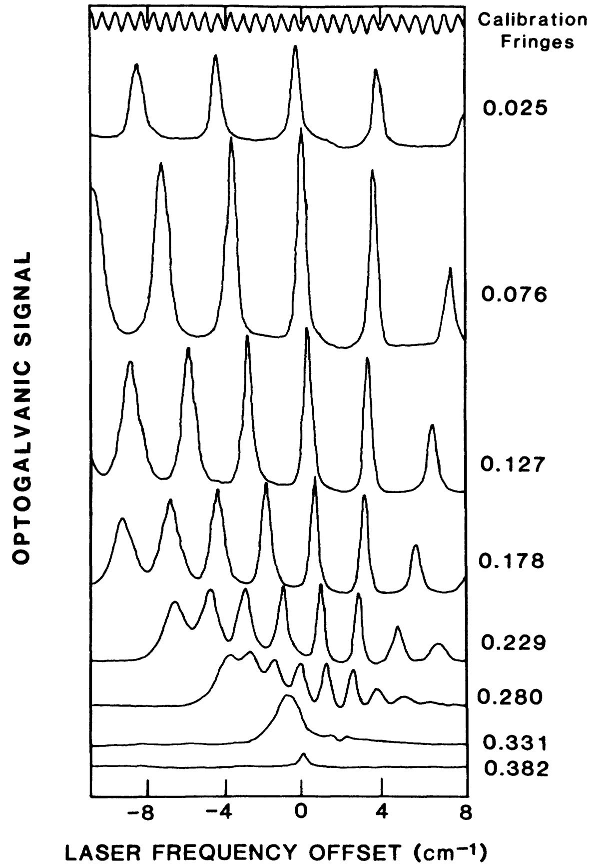

FIG. 3. Optogalvanic Stark spectra in the 3.50-Torr He discharge operating at 1.50 mA/cm^2. The distance from the cathode in centimeters at which each spectra is taken is indicated at the right.

The relative linestrength of Stark components or groups of components is also useful in field measurements.[16] This approach works best at low fields where the linestrengths are strongly dependent on field as indicated in Fig. 2(b). The relative linestrengths are equal at high field. In order to determine an electric field from relative linestrengths one must (1) avoid saturation of experimental spectra and (2) establish that the optogalvanic effect is equally efficient on all components. This second condition can be argued on fairly general grounds. Collisions with ground-state atoms rapidly mix the populations of the zero-field $n=11$ levels. The cross section for l mixing of $n=11$ Na atoms by collision with ground-state He atoms is 1.85×10^3 Å^2.[27] It is reasonable to assume that an $n=11$ He atom behaves similarly to an $n=11$ Na atom, thus the l mixing rate of approximately 4×10^9 sec^{-1} at 3.5 Torr is expected. This mixing rate completely overwhelms radiative decay from the $11\,^1P$ level at a vacuum rate of 1.4×10^7 sec^{-1}.[28] Radiation trapping further strengthens the argument by lowering the effective radiative decay rate. A comparison of relative linestrengths must be based on integrated linestrengths because the spectral widths of the Stark components vary across the manifold. The outer components are broadened by the local electric field gradient. The laser probes some finite volume containing a range of field magnitudes. The spectral position of the outer components is most dependent on the field, and hence their widths is proportional to the field gradient and the volume probed by the laser.

The results of field measurements as a function of position made at five different current densities in 3.5 Torr of He are plotted in Fig. 4. These measurements are based on the splittings of adjacent components and the width of the Stark manifold. The solid lines are linear-least-square fits to the data. The linear decrease in field magnitude with distance from the cathode is in agreement with the classic picture of the cathode-fall region. Close inspection reveals only a very slight negative curvature. This linear behavior persists to quite small fields near the cathode-fall–negative-glow boundary where the field extrapolates to zero. Direct measurements to rather low fields have been reported by Ganguly *et al.*[29] The position of the boundary between the cathode-fall and negative-glow regions can also be confirmed by a qualitative and quantitative change in optogalvanic effects. The excellent agreement between the voltage measured using a digital voltmeter and the voltage determined by integrating the electric field across the cathode-fall region indicates that the field measurements are on average accurate to 1%.

It is essential to determine both the electric field and the E/N throughout the cathode-fall region. We found that significant gas heating and a corresponding gas density reduction occurs in the abnormal cathode-fall region, even with the water-cooled electrodes in our experiment. Ions carry most of the current in the cathode-fall region. The motion of atomic or molecular ions in their parent gas (i.e., He^+ in He or $N_2{}^+$ in N_2) is limited by symmetric charge exchange

$$\mathrm{He}^+(\mathrm{fast})+\mathrm{He}(\mathrm{slow})\rightarrow\mathrm{He}(\mathrm{fast})+\mathrm{He}^+(\mathrm{slow})\ . \tag{4}$$

This reaction has a large resonant cross section which is only weakly dependent on energy. It results in a short equilibration distance for ions as discussed in Sec. IV, and a very efficient conversion of electrical energy to heavy-particle translational motion and to heat. Examination of the typical Nd_c products (gas density times cathode-fall thickness) suggests that many of the energetic neutrals scatter before reaching the cathode.

To complement the field measurements in Fig. 4, the gas temperature is measured in the cathode-fall region for each of the five current densities of the study. The tem-

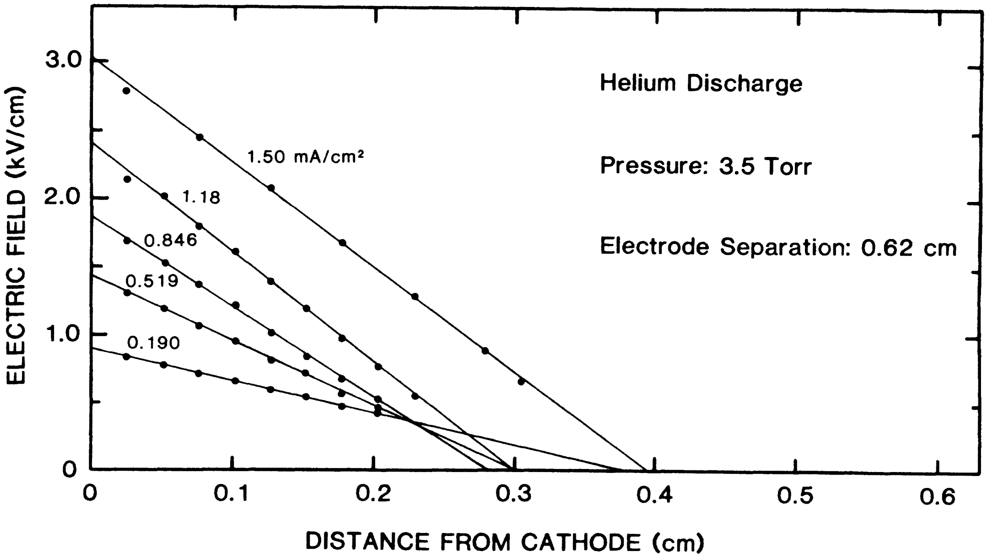

FIG. 4. Electric field as a function of distance from the cathode for five current densities, all at 3.50 Torr. The lines are linear-least-squares fits to the data. The anode corresponds to the right-hand side of the figure.

perature is found to be constant within an error bar throughout the cathode-fall region.

Doppler profiles are obtained by scanning a nonsaturating pulsed dye laser through the transition of interest and detecting the resulting optogalvanic signal with a boxcar averager. The beam was focused to a width of 0.06 cm within the cathode-fall region. The transition is the $2\,^1S$ to $3\,^1P$ transition of He at 501.6 nm. The dye laser bandwidth is reduced to 300 MHz by introducing an étalon. Other contributions to the observed line shape include a natural width of 92 MHz,[28] pressure broadening at 3.5 Torr of 146 MHz,[30] and Stark broadening on the order of 100 MHz. These contributions are small compared to the Doppler width of 3.66 GHz at 293 K.

The temperature was determined by measuring the full width at half maximum intensity of the line profile. Since the temperature increase is proportional to the power dissipated in the discharge and the Doppler width is proportional to the square root of the temperature, the square of the measured width was plotted as a function of discharge power. If the broadening mechanisms, apart from Doppler broadening, are negligible, the resulting extrapolation should indicate a zero-power Doppler width which corresponds to ambient gas temperature. The difference between the width calculated at ambient temperature and that indicated by the zero-power extrapolation gives the residual width, which was then subtracted from the measured widths. This correction is less than the size of the error bar. The temperature at each current density was then determined from the width.

Figure 5 is the resulting experimentally derived gas density as a function of discharge power measured at a constant pressure of 3.50 Torr. At the highest power studied, the density is 30% lower than what would be expected assuming ambient temperature. Each data point is determined from ten Doppler width measurements. These density measurements are combined with the field measurements of Fig. 4 to derive important parameters of the cathode-fall region in Sec. IV of this paper.

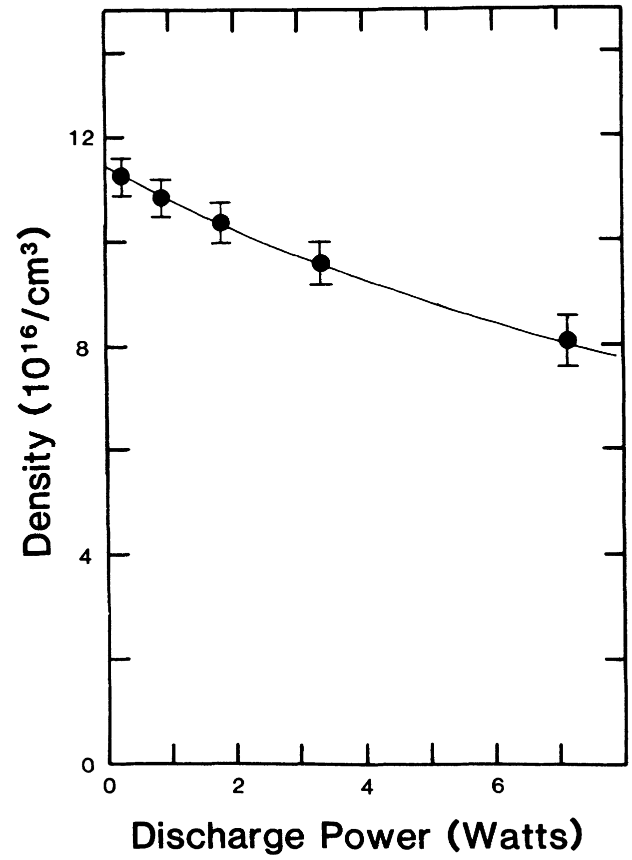

FIG. 5. Experimentally derived gas density as a function of discharge power measured at a constant pressure of 3.50 Torr.

IV. CURRENT BALANCE AT THE CATHODE SURFACE

The current balance at the surface of the cathode is the ratio of the ion current to electron current, which is determined from measurements of the electric field and gas density in the cathode-fall region and the total discharge current density J_D. The ion current density at the cathode, J_+^0, is the product of the ion charge density ρ_+ and the average ion velocity at the cathode surface, $\langle v_z \rangle^0$. Poisson's equation determines the space-energy density in the cathode-fall region from the spatial gradient of the electric field. High fields in the cathode-fall region result in very high electron velocities and a negligible electron density; the space charge is almost entirely due to the ions.

Ion motion in the cathode-fall region is limited by the symmetric charge exchange reaction of Eq. (4). The cold gas or high-field approximation is applicable throughout most of the cathode-fall region. In this approximation the ion is assumed to start from rest after each charge exchange. It is thus reasonable to argue that the equilibration distance of the ions should be comparable to the mean free path for symmetric charge exchange. Each charge exchange collision wipes out all memory of the ion's history. Although the above argument is appealing, two aspects of the cathode-fall region complicate the picture. There is a significant field gradient, and new ions are produced throughout the cathode-fall region by electron-impact ionization.

These complications have both been included in an analytic treatment of ion transport in the cathode-fall region.[31] These solutions to the Boltzmann equation for ions will be summarized here. It is convenient to reverse coordinate systems when discussing ions. In most of this paper, parameters are measured and plotted as a function of distance from the cathode. For this discussion of ion transport we choose an origin at the boundary between the cathode-fall and negative-glow regions, and we let the positive z axis point toward the cathode. This temporary change in coordinate systems makes the field, ion velocity, and ion flux density positive. The time-independent Boltzmann equation is

$$\frac{eE}{m_+}\frac{\partial f}{\partial v_z}+\mathbf{v}\cdot\nabla f = -N\sigma v f + N\sigma\delta(\mathbf{v})\int\int\int f v \, dv_z dv_x dv_y + P(z)\delta(\mathbf{v}) \,, \tag{5}$$

where e is a unit charge, m_+ is the ion mass, σ is the charge exchange cross section, and $P(z)$ is the electron-impact ionization rate per unit volume. The charge exchange cross section, although weakly energy dependent, is here approximated as independent of energy. The first and second terms on the right-hand side of Eq. (5) are Wannier's elegant expression for the collision term due to symmetric charge exchange.[32] The third term is a source term due to electron-impact ionization. This source term and the electric field should come from a self-consistent description of the cathode-fall region which is beyond the scope of this work. We therefore use a field which increases linearly with distance from the cathode-fall–negative-glow boundary and replace the ion acceleration eE/m_+ by kz. The electron-impact ionization rate per unit volume, $P(z)$, is known to peak near the cathode-fall–negative-glow boundary from Monte Carlo simulations by Beouf and Marode, and others.[17] Section VII of this paper describes a determination of $P(z)$ from Monte Carlo simulation of electron avalanches in the cathode region. A lower limit for the equilibration distance is calculated by assuming that $P(z)$ describes a plane source at the cathode-fall–negative-glow boundary. An upper limit for the equilibration distance is calculated by assuming $P(z)$ describes a uniform source for positive z. Both limits are derived from the solution to the problem where $P(z)$ is a plane source $j\delta(z-z_0)$ and where $z_0>0$. The distribution function at any positive z for this source is

$$f_G = j\delta(v_x)\delta(v_y)s(v_z)(\exp[-\sigma N(z-z_0)]2\delta(v_z^2-kz^2+kz_0^2) + (\sigma N/\sqrt{k})[1-s(v_z^2-kz^2+kz_0^2)]\exp\{\sigma N z[(1-v_z^2/kz^2)^{1/2}-1]\}/(kz^2-v_z^2)^{1/2}) \,, \tag{6}$$

where $s(v_z)$ represents a step function. The integral $\int\int\int f_G \mathbf{v}\, dv_z dv_x dv_y$ is the ion flux density $j\hat{z}$ for all z greater than z_0. The flux density must be independent of position by conservation of particles. The integral

$$\int\int\int f_G dv_z dv_x dv_y$$

is the ion density which is dependent on position because the ions are accelerating. The distribution function of Eq. (6) for large z approaches Wannier's equilibrium distribution function[32]

$$f_{\text{eq}} = j\delta(v_x)\delta(v_y)(\sigma N/kz)s(v_z)\exp(-v_z^2\sigma N/2kz) \,. \tag{7}$$

The lower limit for the equilibration distance of ions in the cathode-fall region is determined by letting z_0 approach zero. This limit corresponds to a plane source of ionization at the cathode-fall–negative-glow boundary. The average velocity in the z direction for the case where z_0 approaches zero is

$$\langle v_z\rangle = \frac{\int\int\int f_G v_z dv_z dv_x dv_y}{\int\int\int f_G dv_z dv_x dv_y} = \frac{1}{\exp(-\sigma N z)/\sqrt{k}\,z + \pi\sigma N\exp(-\sigma N z)[I_0(\sigma N z)+L_0(\sigma N z)]/2\sqrt{k}} \,, \tag{8}$$

where $I_0(z)$ is a modified Bessel function of order 0 and $L_0(z)$ is a modified Struve function of order 0 as defined and tabulated in Abramowitz and Stegun.[33,34] The average velocity for this case reaches 90% of the equilibrium drift velocity $\sqrt{2kz/\pi\sigma N}$ in 1.7 mean free paths. If $z_0 \gg (\sigma N)^{-1}$ then the field changes only slightly in a mean free path and the equilibration distance will be that of the constant field problem, $0.65/\sigma N$, or two-thirds of a mean free path.[31]

The flux density, average velocity, and ion density are plotted in Fig. 6 for the distribution function of Eq. (6) with $z_0 \cong 0$. The flux density, plotted in Fig. 6(a), must be independent of z because the source is localized at z_0 near the origin and the system is in steady state. The average velocity, plotted in Fig. 6(b), is a steadily increasing function of z because the field increases linearly with z. Figure 6(c), which is a plot of the ratio of the average velocity to the local equilibrium drift velocity $\sqrt{2kz/\pi\sigma N}$, clearly shows that the nonhydrodynamic behavior is confined to within a few mean free paths of the source near the origin. The equilibration distance of 1.7 mean free paths required for the average velocity to reach 90% of the local equilibrium drift velocity is read directly from Fig. 6(c). A low average velocity near the origin implies a large ion density because their product is the constant flux density. The ion density is plotted in Fig. 6(d).

Equation (6) for f_G is very slightly different from f_3 as defined in Eq. (7) of Ref. 31. The changes make f_G defined (zero) for positive z less than z_0. Thus f_G corresponds more closely to Arfken's definition of a one-dimensional Green's function.[35] The distribution function at any positive z for a linearly increasing field with arbitrary $P(z)$ is

$$f=\delta(v_x)\delta(v_y)s(v_z)$$
$$\times\int_0^{\infty}P(z_0)(\exp[-\sigma N(z-z_0)]2\delta(v_z^2+kz^2-kz_0^2)$$
$$+(\sigma N/\sqrt{k})[1-s(v_z^2-kz^2+kz_0^2)]\exp\{\sigma Nz[(1-v_z^2/kz^2)^{1/2}-1]\}/(kz^2-v_z^2)^{1/2})dz_0\ . \tag{9}$$

This integral determines a realistic ion distribution function if a Monte Carlo simulation of electron avalanches is used to determine $P(z)$, the electron-impact ionization rate per unit volume. A flux density evaluated directly from an exact distribution function includes drift, diffusion, and all higher-order terms of a density gradient expansion. An exact solution may be particularly valuable in modeling an abrupt cathode-fall negative-glow boundary. The objective here is to prove that the average ion velocity is the equilibrium drift velocity in most of the cathode-fall region. The true source function as determined in Monte Carlo simulations peaks near the cathode-fall–negative-glow boundary, and thus is a decreasing function of z throughout the cathode-fall region. The upper limit on the equilibration distance is determined by using a uniform ionization rate per unit volume for all positive z. The average ion velocity for a linearly increasing field with a uniform source of ions or all positive z is

$$\langle v_z\rangle=\frac{\int\int\int f v_z dv_z dv_x dv_y}{\int\int\int f\, dv_z dv_x dv_y}$$
$$=\frac{z}{\exp(-\sigma Nz)\pi\{I_0(\sigma Nz)+L_0(\sigma Nz)+\sigma Nz[I_1(\sigma Nz)+L_1(\sigma Nz)+2/\pi]\}/(2\sqrt{k})}\ , \tag{10}$$

where $I_1(z)$ and $L_1(z)$ are modified Bessel and modified Struve functions of order 1.[33,34] The distance required for the average velocity to reach 90% of the equilibrium drift velocity $\sqrt{2kz/\pi\sigma N}$ is 5.7 mean free paths.

The ratio of the thickness of the cathode-fall region d_c, to the mean free path for symmetric charge exchange $(\sigma N)^{-1}$ is typically 50 to 100 for a rare-gas cathode fall. A change in discharge current or pressure changes Nd_c only slightly, thus the observation

$$\sigma Nd_c \gg 5.7 \tag{11}$$

justifies using an equilibrium ion drift velocity in nearly all of the cathode-fall region. The approximation fails only within the first six mean free paths from the cathode-fall–negative-glow boundary. The preceding proof that the ions are in hydrodynamic equilibrium enables us to complete the determination of the current balance at the surface of the cathode.

The drift velocity at the cathode surface for low currents is determined from Helm's precise mobility data.[36] At the high current densities the drift velocity is calculated using the equilibrium expression

$$\langle v_z\rangle^0=[2eE^0/(m_+\pi\sigma N)]^{1/2}\ , \tag{12}$$

where E^0 is the field at the cathode surface. The symmetric charge exchange cross section σ is taken from the calculation of Sinha, Lin, and Bardsley.[37] These calculations agree with Helm's experimentally derived cross sections. The slight energy dependence of σ does not weaken the proof of equilibration, but it is important to use a value of σ that corresponds to the average ion energy at the cathode surface. The average ion energy at the cathode from the equilibrium distribution function of Eq. (7) is

$$\langle m_+v_z^2/2\rangle^0=eE^0/2N\sigma\ . \tag{13}$$

A self-consistent average ion energy and symmetric charge exchange cross section are conveniently determined from a graphical analysis using a plot of σ versus ion energy. The intersection of the σ versus ion energy

TABLE I. Summary of the analysis of the electric field and gas density measurements to determine the current balance at the cathode surface. The dimensionless ratio $J_+^0/(J_D-J_+^0)$ is the number of ions produced in the cathode-fall region per (net) electron emitted from the cathode.

	J_D (mA/cm^2)				
	0.190	0.519	0.846	1.18	1.50
E^0 (kV/cm)	0.897	1.426	1.870	2.395	3.017
d_c (cm)	0.382	0.301	0.282	0.300	0.396
V_{vm} (kV)	0.173	0.211	0.261	0.356	0.600
V_{ef} (kV)	0.171	0.215	0.264	0.359	0.597
N (10^{16} cm^{-3})	11.2	10.8	10.3	9.48	8.01
ρ_+ (10^{-10} C/cm^3)	2.08	4.20	5.88	7.07	6.74
$\langle m_+v_z^2/2\rangle^0$ (eV)	1.66	2.82	3.89	5.71	8.92
σ (10^{-16} cm^2)			23.3	22.1	21.1
$\langle v_z\rangle^0$ (10^5 cm/sec)	7.12	9.28	10.9	13.2	16.5
J_+^0 (mA/cm^2)	0.148	0.390	0.641	0.933	1.11
$J_+^0/(J_D-J_+^0)$	3.52	3.02	3.13	3.78	2.85

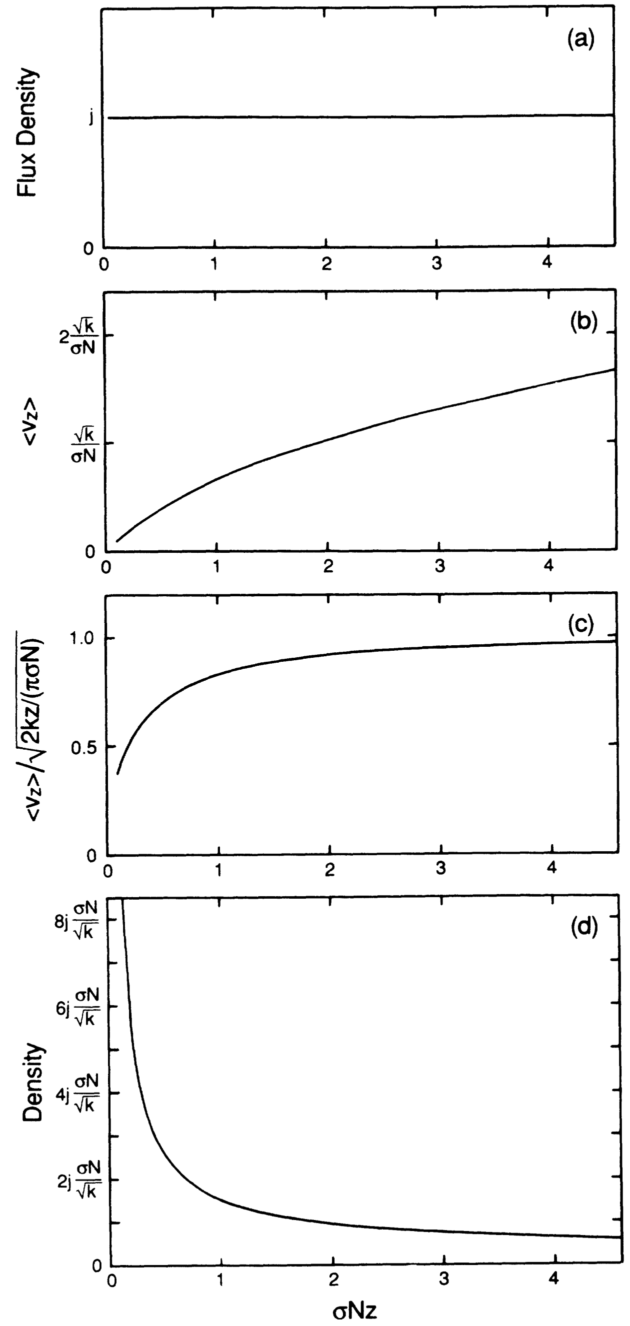

FIG. 6. Integrals of the Eq. (6) distribution function vs the number of mean free paths from the source at z_0 near the origin: (a) flux density, (b) average velocity, (c) ratio of average velocity to local equilibrium drift velocity, (d) density.

plot with a hyperbola defined by Eq. (13) and an empirical E^0/N determines the self-consistent average ion energy and symmetric charge exchange cross section. The uncertainty in $\langle v_z \rangle^0$ is ±4% in all cases.

Table I summarizes the analysis of the electric field and gas density measurements to determine the current balance at the cathode surface. The excellent agreement between V_{vm}, a voltage determined with a digital voltmeter, and V_{ef}, a voltage determined from integrating the field data, indicates that the field measurements are on the average accurate to 1%. The uncertainty in the ion charge density ρ_+ is comparable to the uncertainty in the field measurements. The electron current density at the cathode surface is $J_D - J_+^0$ where J_D is the discharge current density. The electron current density has, of course, a larger fractional uncertainty than the ion current density. The dimensionless ratio $J_+^0/(J_D - J_+^0)$ is the current balance or ratio of the ion current to electron current at the cathode surface. This ratio is of particular interest because it is the number of ions produced in the cathode-fall region per (net) electron emitted from the cathode.

V. METASTABLE DENSITY MEASUREMENTS

The spatial dependence of $2\,^1S$ and $2\,^3S$ He metastable densities is mapped along the axis of the discharge for each of the five current densities. The experiment has two parts: (1) laser-induced fluorescence is used to create spatial maps of relative metastable densities and (2) absorption measurements are used to put an absolute scale on the density maps. The absolute density of metastables is modeled in Sec. VI to derive metastable production rates for comparison to Monte Carlo simulations. From the spatial distribution of metastables, and specifically from the suppression of $2\,^1S$ metastables in the negative glow, valuable information is gained about the low-energy electrons in the negative glow.

Laser-induced fluorescence is the best detection method for producing relative maps of the metastable density. Although optogalvanic detection offers superior sensitivity near the cathode surface, its sensitivity is position dependent. The laser-induced fluorescence measurements are made using a pulsed N_2 laser pumped dye laser tuned to either the 501.6-nm transition for mapping the $2\,^1S$ density or the 388.9-nm transition for mapping the $2\,^3S$ density. The beam passes through a 250-μm slit which was imaged 1:1 into the center of the discharge using a 13-cm-focal-length cylindrical lens. The laser polarization is along the axis of the discharge. Fluorescence is collected in a direction mutually perpendicular to the laser axis and the axis of the discharge. The fluorescence collection system includes a lens and slit combination to isolate the central portion of the laser-discharge interaction region. This eliminates possible distortion of the spatial map due to metastable populations in the fringes. The lens is masked to cut down on fluorescence scattered from electrodes which can also distort the map.

Excitation transfer among the $n=3$ levels due to collisions with ground-state atoms allows the monitoring of fluorescence at a wavelength different from that of the laser.[38] Interference filters are used to isolate 667.8-nm ($3\,^1D - 2\,^1P$) radiation when the laser is tuned to 501.6- and 706.5-nm ($3\,^3S - 2\,^3P$) radiation when the laser is tuned to 388.9 nm. In this way scattered laser light is eliminated from the signal. The fluorescence is detected with a photomultiplier. The signal is averaged over ~1000 laser pulses. The entire fluorescence collection system is mounted on the translation stage so it remains fixed with respect to the discharge.

The laser absorption measurements for determining an absolute scale for the metastable densities are made using the same transitions as the laser-induced fluorescence studies. Although absorption detection is far less sensitive than optogalvanic or fluorescence detection, it does provide a convenient absolute scale. An étalon is introduced to reduce the laser bandwidth to 500 MHz and thereby simplify analysis of the absorption data. The beam passes through a 500-μm slit which is imaged 1:1 into the discharge. Absorption measurements are made at the peak of the spatial density at two current densities. The intensity of the laser is substantially reduced to avoid saturation of the transition. The transmitted laser light is monitored with a photodiode detector. The signal from the detector is processed with a boxcar averager and plotted on a strip-chart recorder as the laser is scanned through the transition. Metastable densities are determined from the integral over frequency of the natural log of the transmittance. Each density is an average of ten measurements.

Figures 7 and 8 show the results of the metastable density measurements. The density maps have an uncertainty of $\sim 20\%$ in the center of the discharge rising to $\sim 30\%$ near the electrodes.

VI. METASTABLE TRANSPORT AND KINETICS

The metastable maps of Sec. V are analyzed in this section. The transport and kinetics of $2\,^1S$ and $2\,^3S$ metastables in the discharge are modeled using a pair of balance equations which are coupled differential equations,

$$D_s\frac{\partial^2 M_s}{\partial z^2}-\beta M_s^2-\beta M_s M_t-\gamma M_s N-\kappa n_e M_s+P_s=0\ , \tag{14}$$

$$D_t\frac{\partial^2 M_t}{\partial z^2}-\beta M_t^2-\beta M_s M_t+\kappa n_e M_s+P_t=0\ , \tag{15}$$

where $M_{s,t}$ is the metastable density, N is the density of ground-state atoms, n_e is the density of low-energy electrons, D is the diffusion coefficient, P is the production rate per unit volume, γ is the rate constant for singlet metastable destruction due to collisions with ground-state atoms, β is the rate constant for destruction of metastables due to metastable-metastable collisions, κ is the effective rate constant for destruction of singlet metastables due to low-energy electron collisions, and s and t subscripts indicate singlet and triplet metastables, respectively. The first three terms in each equation are loss terms arising from diffusion and collisions between metastables. There is an additional loss term in the singlet equation due to collisions with ground-state He atoms. The marked suppression of singlet metastables in the negative glow is due to low-energy electron collisions, i.e. the reactions

$$\mathrm{He}(2\,^1S)+e^-\rightarrow\mathrm{He}(2\,^3S)+e^-+0.79\ \mathrm{eV}\ , \tag{16a}$$

$$\rightarrow\mathrm{He}(2\,^1P)+e^--0.60\ \mathrm{eV}\ . \tag{16b}$$

These reactions both have large cross sections. Exothermic reaction (16a) is a spin exchange, s-wave process with a large cross section for low-energy electrons. Endothermic reaction (16b) corresponds to a very strong optically allowed transition; it has a large cross section peaking at electron energies roughly three times thresh-

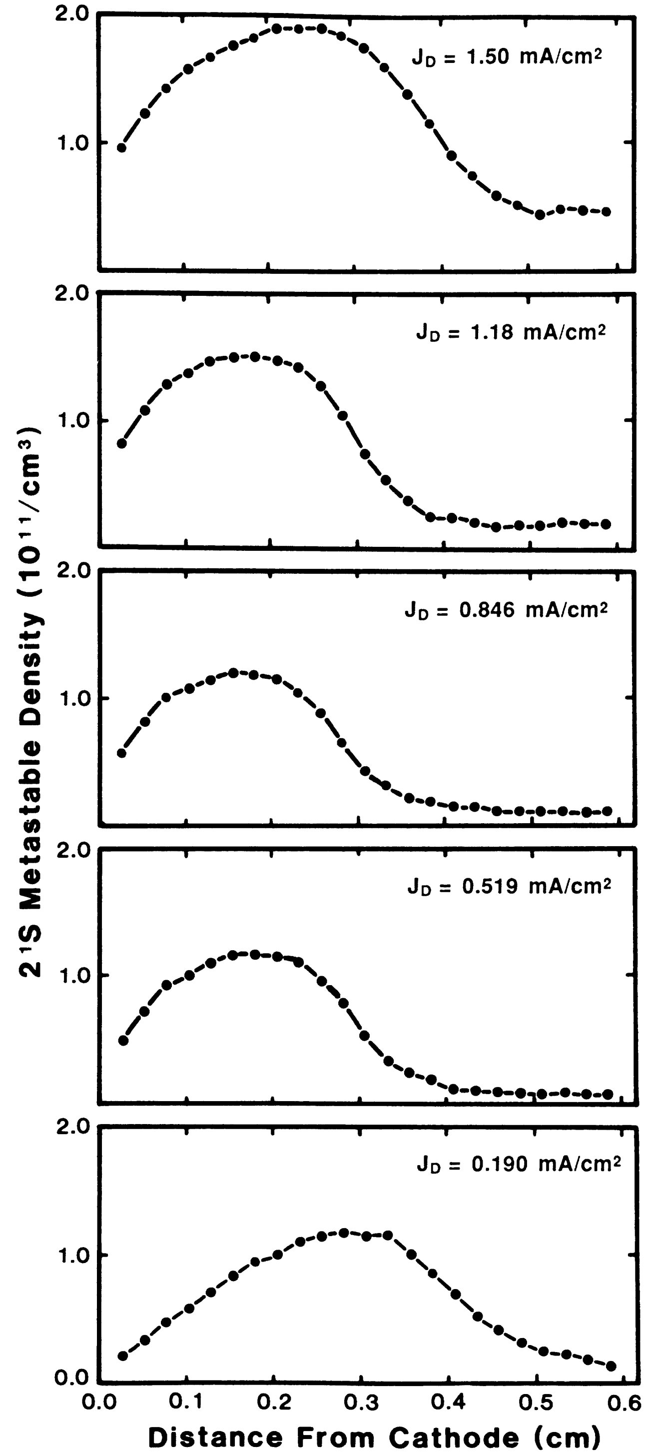

FIG. 7. Helium $2\,^1S$ metastable density as a function of distance from the cathode for five discharge current densities at 3.50 Torr.

old energy. Reaction (16a) dominates the $2\,^1S$ quenching, because (16b) must compete with the $2\,^1P \rightarrow 2\,^1S$ radiative decay. The metastable spin conversion reaction (16a) is included as the fifth loss term in the singlet equation and a corresponding gain in the triplet equation.

Low-energy electrons are confined to the negative-glow region due to the high fields in the cathode-fall region. The spatial dependence of the low-energy electron density n_e is therefore that of a step function; it is zero in the cathode-fall region, rising sharply at the negative-glow boundary to some constant value. The spatial dependence of the production terms is assumed to be a fundamental diffusion mode except at the highest and lowest currents where the fundamental mode is skewed slightly to maintain the peak at the cathode-fall–negative-glow boundary. The assumption that the production peaks at the boundary is borne out by Monte Carlo simulations discussed later in this paper. Values for DN, γ, and β are taken from Phelps.[39] The temperature dependence of D is taken from Buckingham and Dalgarno,[40] that of γ is taken from Allison, Browne, and Dalgarno.[41]

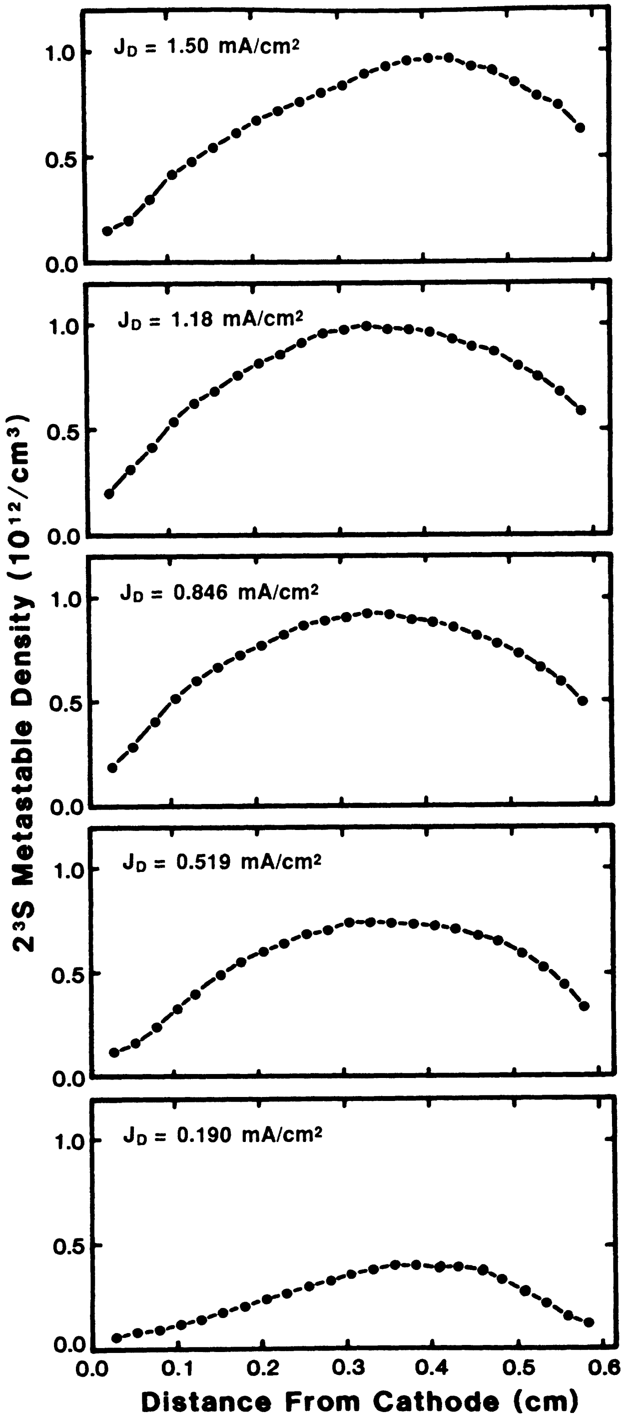

FIG. 8. Helium $2\,^3S$ metastable density as a function of distance from the cathode for five discharge current densities at 3.50 Torr.

The key quantities which are determined in this modeling are the integrated production rates, $\int P_s dz$ and $\int P_t dz$, and the product of the rate constant for metastable spin conversion with the low-energy electron density, κn_e. Values for these key quantities are assumed, the coupled equations are solved for $M_s(z)$ and $M_t(z)$, and a comparison is made to the empirical metastable density maps. Diffusion modes up to tenth order are included in the solutions because of the spatial asymmetry introduced by metastable spin conversion. After the comparison with the empirical metastable maps, the values for $\int P_s dz$, $\int P_t dz$, and κn_e are adjusted and the processes iterated until a good fit to the empirical metastable maps is achieved. The value for κn_e determined in this fashion should be considered an effective rate of metastable spin conversion because it must be modified to include the reverse reaction. The reverse reaction is not negligible if the relative singlet versus triplet metastable density approaches thermal equilibrium with the low-energy electron gas in the negative glow.

Figures 9 and 10 show both the measured and calculated $2\,^1S$ and $2\,^3S$ densities, respectively, for one of the current densities. Table II summarizes for all current densities the parameters used in the model such as D_s, D_t, γ, and β and the key quantities $\int P_s dz$, $\int P_t dz$, and κn_e. The dimensionless ratios

$$e\int P_s dz/(J_D - J_+^0), \quad e\int P_t dz/(J_D - J_+^0),$$

where $J_D - J_+^0$ is the empirical electron current density at the cathode, are of particular interest. These dimensionless ratios are the average number of singlet and triplet metastables produced per (net) electron emitted from the cathode.

VII. MONTE CARLO SIMULATIONS

Monte Carlo simulations are used in this work to study electron avalanches in the cathode-fall and negative-glow regions. There is no need for Monte Carlo simulations of ion transport in the cathode-fall region because we have the exact analytic solutions to the Boltzmann equation for ions as presented in Sec. IV. The Monte Carlo simulations are used to determine the number of ions and metastable atoms produced per (net) electron emitted from the cathode. The number of ions produced in the

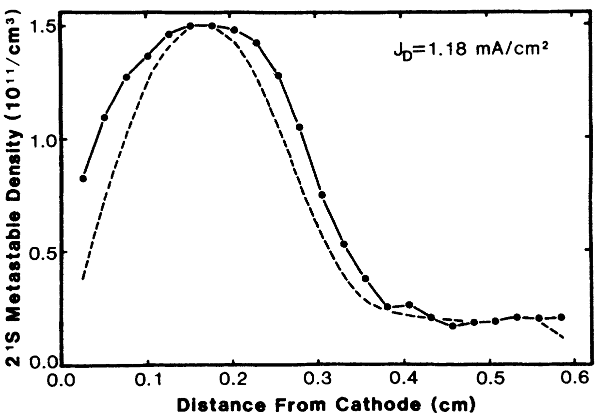

FIG. 9. Helium $2\,^1S$ metastable density for $J_D=1.18$ mA/cm^2. The points are the experimental data and the dashed curve is the calculated fit to the data.

cathode-fall region per emitted electron is directly comparable to the empirical current balance of Sec. IV. The number of metastables produced is comparable to the results of Sec. VI.

The Monte Carlo simulations include the empirical field distributions and gas densities for the cathode-fall region as given in Sec. III. A uniform field of 1.0 or 10.0 V/cm is assumed for the negative-glow region. We believe that there is actually a reversal of the field direction at the boundary between the cathode-fall and negative-glow regions. The reversal would produce a potential-energy well which holds the low-energy electron gas of the negative glow. The reversal would also result in a backdiffusion (or drift) toward the anode of ions produced in the negative glow. Unfortunately it is difficult to include a field reversal in the Monte Carlo simulations. However, the actual magnitude and direction of the weak field in the negative-glow region has very little effect on

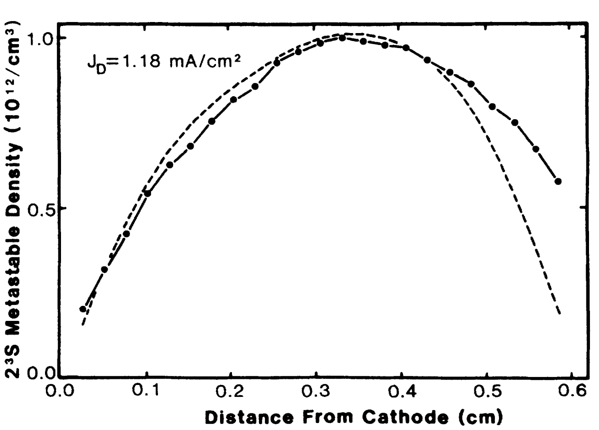

FIG. 10. Helium $2\,^3S$ metastable density for $J_D=1.18$ mA/cm^2. The points are the experimental data and the dashed curve is the calculated fit to the data.

excitation and ionization in the negative glow which is produced by high-energy beam electrons from the cathode-fall region.

The Monte Carlo simulations are three dimensional in the sense that they include angular scattering, but they do not include edge effects due to fringing of the discharge. One-dimensional infinite plane parallel geometry is assumed. Null collision techniques eliminate most of the time-consuming numerical integration in Monte Carlo simulations. The null collision technique used in this investigation was developed by Boeuf and Marode for nonuniform fields.[17] An interested reader will find more detail on the Monte Carlo technique in Ref. 17. The simulations include anisotropic elastic scattering, excitation to 22 levels, direct ionization, and other less important processes.

Total and differential elastic scattering cross sections are taken from the calculations of LaBahn and Callaway.[2] The analytic expressions given by Alkhazov for excitation cross sections are used in the simulations.[43] Excitation of $n=2$ to 5 singlet and triplet s and p levels is included in the simulation. Excitation of the $n=3$ to 5 singlet and triplet d levels is also included. Although some experimental or theoretical information on differential excitation cross sections for electrons on He is available, it is rather limited. Thus we use an isotropic scattering approximation for excitation.

A fraction of the atoms excited to the $3p$ levels and above are associatively ionized. An accurate determination of the fraction requires accurate associative ionization cross sections, cross sections for excitation transfer due to ground-state atom collisions, and radiative decay rates. On the basis of what information is available we estimate that 25% of the atoms in the $3p$ levels and above are associatively ionized at 3.5 Torr.[28,38] The electrons released in associative ionization contribute to the avalanche; they are assumed to have an initial kinetic energy of 1.0 eV and an isotropic angular distribution. The remaining 75% of the atoms excited to the $3p$ and higher triplet levels, and all of the atoms excited to the $3\,^3S$ and $2\,^3P$ levels are assumed to radiate to the $2\,^3S$ metastable level. This cascade contribution is combined with direct excitation of the $2\,^3S$ level to determine the total production rate for $2\,^3S$ metastables. The total production rate for $2\,^1S$ metastables includes direct excitation and a cascade contribution of 19% of the excitation to the $3p$ and higher singlet levels. The total production rate for the $2\,^1P$ resonant level includes direct excitation and a cascade contribution of all of the $3\,^1S$ excitation and 56% of the excitation to the $3p$ and higher singlet levels. These assumptions are based on a significant l mixing of $3p$ and higher level populations due to collision with ground-state atoms.

In a vacuum nearly all of the atoms excited to the $2\,^1P$ resonant level decay to the ground state via vuv emission. Radiation trapping reduces the effective decay rate to 1.3×10^6 sec^{-1}, which is comparable to the vacuum decay rate of 1.98×10^6 sec^{-1} for the $2\,^1P\rightarrow2\,^1S$ infrared branch at 2 μm.[28] However, the $2\,^1P\rightarrow2\,^1S$ branch is also trapped in the cathode-fall region of our discharge experiments, thus we do not include any of the $2\,^1P$ exci-

TABLE II. Summary for all current densities of parameters used in the model as well as the key quantities $\int P_s dz$, $\int P_t dz$, and κn_e. The dimensionless ratios $e\int P_s dz/(J_D - J_+^0)$ and $e\int P_t dz/(J_D - J_+^0)$ are the average number of singlet and triplet metastables produced per (net) electron emitted from the cathode.

	J_D (mA/cm^2)				
	0.190	0.519	0.846	1.18	1.50
N (10^{16} cm^{-3})	11.2	10.8	10.3	9.48	8.01
D_s (cm^2/sec)	127	140	152	173	236
D_t (cm^2/sec)	136	150	163	185	253
γ (10^{-15} cm^3/sec)	6.0	6.5	6.9	7.8	9.9
β (10^{-9} cm^2/sec)	3.5	3.5	3.5	3.5	3.5
$\int P_s dz$ (10^{15} cm^{-2}sec^{-1})	0.454	0.664	0.830	1.05	1.38
$\int P_t dz$ (10^{15} cm^{-2}sec^{-1})	0.711	1.86	2.77	3.56	4.34
$e\int P_s dz/(J_D - J_+^0)$	1.73	0.824	0.648	0.680	0.566
$e\int P_t dz/(J_D - J_+^0)$	2.71	2.31	2.16	2.31	1.78
κn_e (10^4 sec^{-1})	1.5	8.5	7.0	5.5	3.0

tation in calculating a total production rate for $2\,^1S$ metastables. This approximation is not completely satisfactory because the $2\,^1P \rightarrow 2\,^1S$ branch is not highly trapped in the negative glow where the $2\,^1S$ density is suppressed by low-energy electron collision. The $2\,^1P$ level is feeding population to the $2\,^1S$ level through a collisional-radiative coupling, and the $2\,^1S$ level is feeding population to the $2\,^3S$ through a collisional coupling. The net result is that the Monte Carlo simulation produces a metastable production rate which is somewhat lower than the empirical rate.

The analytic expression by Alkhazov for the total ionization cross section is used in the simulation.[43] We also use Alkhazov's analytic expression for the differential cross section with respect to energy.[43] Simulations are performed using two different angular distributions for ionizing collisions.

The first simulations assumed isotropic angular distributions for both outgoing electrons in an ionizing collision. Some of the results based on the isotropic angular distribution or ionizing collisions were presented in a recent Letter.[44] The first simulations predicted a current balance in good agreement with experiment in a near-normal cathode-fall region, but predicted too much ionization in a highly abnormal cathode-fall region. The E/N reaches 3000 Td (townsend) in the abnormal cathode-fall region, thus the inelastic processes are resulting in forward peaked angular scattering distributions. Numerical solutions of the Boltzmann equation for electrons have traditionally assumed isotropic angular distributions for inelastic collisions. Recent work by Phelps and Pitchford explores the effect of anisotropic inelastic scattering at very high E/N in N_2.[45]

Our second simulations use the assumptions used by Boeuf and Marode: (1) the incident, scattered, and ejected electron velocities are coplanar, and (2) the scattered and ejected electron velocities are perpendicular with zero net transverse momentum.[17] The justification for these assumptions is not strong, but it does represent a reasonable attempt to introduce anisotropic scattering in ionizing collisions.

The details of the electron interactions with the cathode and anode must be specified. The kinetic energy of electrons emitted from the cathode is assumed to be 5.0 eV and they are assumed to have a random angular distribution in the forward direction. The use of a more realistic energy distribution for electrons emitted at the cathode does not affect ionization or excitation in the Monte Carlo simulations. Some electrons are reflected back to the cathode by elastic scattering from He atoms before they suffer an inelastic collision. Electrons do not have sufficient total energy to reach the cathode after an inelastic collision. The percentage of the gross electron emission which is backscattered to the cathode varies from 19% at the lowest current density (a near-normal cathode fall) to 3.6% at the highest current density (a highly abnormal cathode fall). All Monte Carlo results are presented in terms of net electron emission from the cathode. The Monte Carlo simulation assumes no reflection from the anode; each electron is absorbed immediately when it reaches the anode. This approximation will cause the Monte Carlo simulation to predict excitation and ionization rates in the negative glow which are lower than those in experiment. The discordance is significant only in the case of the highly abnormal glow discharge at 1.50 mA/cm^2.

Figure 11 includes Monte Carlo histograms giving the number of ionization and excitation events per (net) electron emitted from the cathode as a function of distance from the cathode. The results of Fig. 11 are based on the anisotropic angular distribution for ionizing collisions. These histograms are for field distributions and gas densities corresponding to 0.519 mA/cm^2. The spatial dependences of the ionization and excitation rates are all described by a roughly symmetric function which peaks near the cathode-fall–negative-glow boundary. The simulations show that the beam electrons in He penetrate beyond the cathode-fall–negative-glow boundary by a distance comparable to d_c, the thickness of the high-field cathode-fall region. The penetration distance will scale as the inverse of the gas density in a fashion similar to d_c. The $2\,^3S$ metastable excitation has the most asymmetric

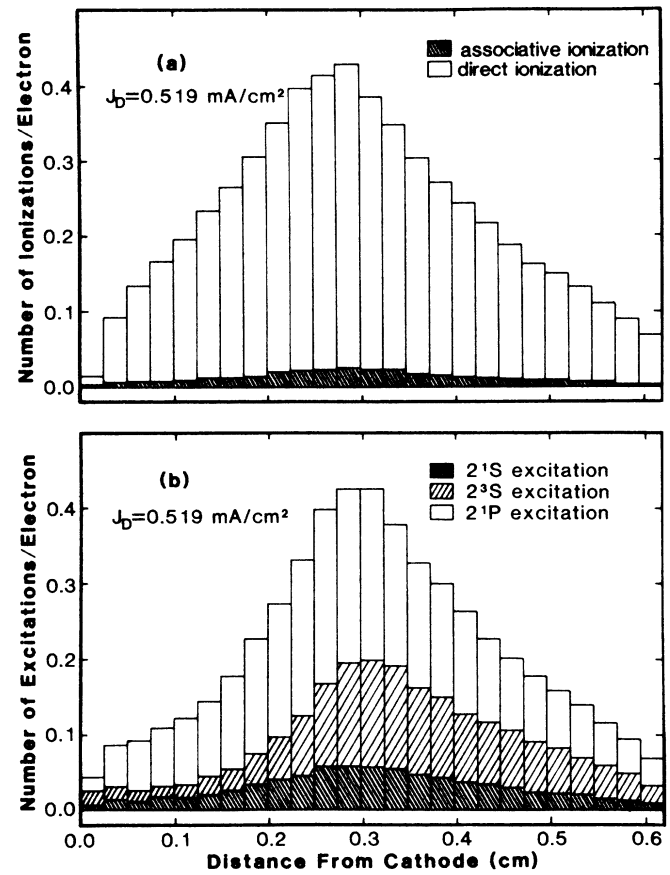

FIG. 11. Monte Carlo histograms showing the number of (a) ionization events and (b) excitation events per (net) electron emitted from the cathode as a function of distance from the cathode. The histogram for total excitation is subdivided into $2\,^1S$, $2\,^3S$, and $2\,^1P$ excitation. The histogram for total ionization is subdivided into associative and direct ionization.

spatial dependence; it is stronger in the negative-glow than in the cathode-fall region. This is explained by the sharp peak just above threshold in the energy dependence of triplet excitation cross sections. The asymmetry in the empirical maps of the $2\,^3S$ metastable density is due in part to the spatial dependence of triplet excitation. The spatial dependences of excitation and ionization at other discharge current densities are similar. The results of Monte Carlo simulations for all five current densities are presented in Tables III and IV. The Table III results are based on the isotropic angular distribution for ionizing collisions, and those of Table IV are based on the anisotropic angular distribution for ionizing collisions.

The absolute accuracy of the Monte Carlo simulations must be estimated in order to compare the simulations to experiment. Statistical uncertainty is not large because several thousand complete avalanches were simulated for each of the five discharge currents. Alkhazov's analytic expressions for the He cross sections are based on theoretical and experimental work by many groups.[43] He estimates that the uncertainty is ±25% at low energy, and ±5% at high energy where a Born approximation is reliable. We believe his uncertainties are reasonable and we estimate that the Monte Carlo results have an uncertainty of ±25%.

VIII. COMPARISON OF EXPERIMENTAL RESULTS AND MONTE CARLO SIMULATIONS

The first comparison of experimental results to Monte Carlo simulations involves the current balance at the cathode. This dimensionless quantity is the ratio of ion to electron current at the cathode. Figure 12 is a plot of the ratio versus total discharge current density. The experimental measurements are points with uncertainties which are discussed in Sec. IV. The dashed line is the same ratio determined from Monte Carlo simulations using the isotropic angular distribution for ionizing collisions. The calculations represented by the dashed line were included in a recent Letter.[44] The solid line is the ratio as determined from Monte Carlo simulations using the anisotropic angular distribution for ionizing collisions. All Monte Carlo simulations include the same anisotropic elastic scattering. Clearly the assumption of isotropic inelastic scattering is beginning to fail in the highly abnormal cathode-fall region where E/N reaches 3000 Td.

TABLE III. Results of Monte Carlo simulations of electron avalanches based on the isotropic angular distribution for ionizing collisions. All results are per (net) electron emitted from the cathode. The ionization in the cathode-fall region includes direct plus associative ionization occurring between the surface of the cathode and a distance d_c from the cathode. Other quantities include all events between the cathode and anode.

	J_D (mA/cm^2)				
	0.190	0.519	0.846	1.18	1.50
E^0 (kV/cm)	0.897	1.426	1.870	2.395	3.017
d_c (cm)	0.382	0.301	0.282	0.300	0.396
N (10^{16} cm^{-3})	11.2	10.8	10.3	9.48	8.01
$2\,^1S$ production	0.88	0.88	0.99	1.06	0.96
$2\,^3S$ production	2.05	1.92	2.04	2.04	1.62
$2\,^1P$ production	3.06	3.37	3.91	4.50	4.51
Associative ionization	0.36	0.38	0.42	0.47	0.49
Direct ionization	4.70	5.98	7.31	9.02	9.84
Ionization in the cathode-fall region	3.89	3.77	4.06	4.52	5.71

TABLE IV. Results of Monte Carlo simulations of electron avalanches based on the anisotropic angular distribution for ionizing collisions. The quantity $\langle T_{\mathrm{an}} \rangle$ is the average kinetic energy of electrons hitting the anode. Other quantities are per (net) electron emitted from the cathode.

	J_D (mA/cm^2)				
	0.190	0.519	0.846	1.18	1.50
E^0 (kV/cm)	0.897	1.426	1.870	2.395	3.017
d_c (cm)	0.382	0.301	0.282	0.300	0.396
N (10^{16} cm^{-3})	11.2	10.8	10.3	9.48	8.01
$2\,^1S$ production	0.77	0.75	0.75	0.74	0.53
$2\,^3S$ production	1.79	1.58	1.52	1.40	0.83
$2\,^1P$ production	2.82	2.98	3.14	3.28	2.51
Associative ionization	0.29	0.31	0.32	0.34	0.25
Direct ionization	4.37	5.37	6.13	6.88	5.86
$\langle T_{\mathrm{an}} \rangle$ (eV)	14.0	16.7	21.8	36.5	106.5
Ionization in the cathode-fall region	3.40	3.10	2.97	3.11	3.24

The current balance from the Monte Carlo simulations includes direct electron-impact ionization and associative ionization due to collisions between highly excited and ground-state He atoms. Ionization from collisions between pairs of metastable atoms is not included, but it is a small ($\leq 10\%$) contribution to the current balance from the Monte Carlo simulations.

The key issue in interpreting the Monte Carlo results is whether or not one should include any of the ionization produced in the negative glow when computing the ratio of the ion to electron current at the cathode. We maintained in a recent Letter, and we continue to maintain, that essentially none of the ionization produced in the negative glow contributes to the ion current at the cathode.[44] The ratio of the ion to electron current at the cathode is computed by summing ionization in spatial bins of a Monte Carlo histogram such as that of Fig. 11. The sum includes spatial bins from the cathode to a distance d_c from the cathode where the cathode-fall–negative-glow boundary occurs. The inclusion of ions produced in the negative glow results in a serious discordance between the current balance determined from the Monte Carlo simulations and the empirical current balance.

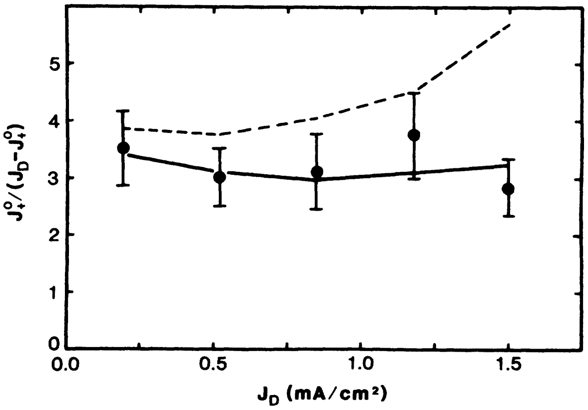

FIG. 12. Ratio of ion current to electron current at the cathode surface $J_+^0/(J_D-J_+^0)$ as a function of discharge current density. The points are the empirically derived values; the dashed line is the Monte Carlo results assuming the isotropic scattering for ionizing collisions; the solid line is the Monte Carlo results incorporating the anisotropic scattering for ionizing collisions.

The issue of the ion current at the cathode-fall–negative-glow boundary was already old and (in)famous when Druyvesteyn and Penning wrote their 1940 review.[46] They did not take a position on the problem in their review. Many experimental and theoretical studies addressed this problem in more recent decades. Long, for example, has a detailed discussion.[2] He argues convincingly for a field reversal in the negative glow, but does not specify the location of the field reversal. He does not take a definite position on the ion current at the cathode-fall–negative-glow boundary. Emeleus devotes an entire section of his 1981 review to the cathode-fall–negative-glow boundary or Glimmsaum, as he calls it.[6] He also fails to take a definite position on the importance of the ion current at the boundary.[6] The strongest position was taken by Little and von Engel.[47] Our arguments, which involve the empirical current balance and Monte Carlo simulations, are not the same as the arguments of Little and von Engels. Our position agrees with that of Little and von Engel. The ion current is a negligible fraction of the discharge current at the cathode-fall–negative-glow boundary. The loss mechanism needed to balance ion production in the negative glow will be discussed in Sec. IX.

The current balance, typically 3.3, is lower than we first expected. It is also surprisingly independent of total discharge current. The greater electric field and thickness in the cathode-fall region at high current are offset by a gas density reduction due to heating. The net result is that on average an electron produces the same amount of ionization in the cathode-fall region at low and high discharge currents. A current balance of 3.3 may be typical of only He.

The second comparison involves the number of metastable atoms produced in the cathode-fall and negative-glow regions per (net) electron emitted from the cathode. The experimental measurements are plotted as points in Fig. 13. The empirical metastable production in units of $\mathrm{cm}^{-2}\,\mathrm{sec}^{-1}$ is divided by the empirical electron flux density at the cathode $(J_D - J_+^0)/e$. The error bars reflect only uncertainties in the metastable density measurements as discussed in Sec. V. The solid line of Fig. 13 is the result of Monte Carlo simulations using the anisotropic angular distribution for ionizing collisions. The $2\,^1S$ production plotted in Fig. 13(a) shows excellent agreement between experiment and the Monte Carlo simulations except at 0.190 mA/cm^2. The discordance in the near-normal glow discharge at 0.190 mA/cm^2 is in part due to the neglect of the $2\,^1P \rightarrow 2\,^1S$ cascade contribution in Monte Carlo determinations of $2\,^1S$ production. At low current densities the $2\,^1P \rightarrow 2\,^1S$ radiation is not completely trapped. The experimental $2\,^3S$ production plotted in Fig. 13(b) is somewhat higher than that predicted by the Monte Carlo simulations. The total $2\,^1S$ and $2\,^3S$ metastable production plotted in Fig. 13(c) is also somewhat higher than that predicted by the Monte Carlo simulations. At least two effects are responsible. The experimental $2\,^3S$ production and the total metastable production are enhanced by a collisional-radiative coupling in the negative glow of the $2\,^1P$ population to the $2\,^1S$ and indirectly to the $2\,^3S$. Some of the $2\,^1P$ production results in metastable production. The disagreement in the highly abnormal glow discharge of 1.50 mA/cm^2 is in part due to the assumption of no electron reflection from the anode. The Monte Carlo results summarized in Table IV show a very high average kinetic energy (>100 eV) for electrons hitting the anode in the highly abnormal glow discharge. Some of these electrons should be reflected at the anode. The reflection from the anode will increase excitation and ionization in the negative glow and improve agreement on metastable production between the experiment and Monte Carlo simulations. The reflection will not significantly change the current balance because few of the reflected electrons will return to the cathode-fall region and produce ionization.

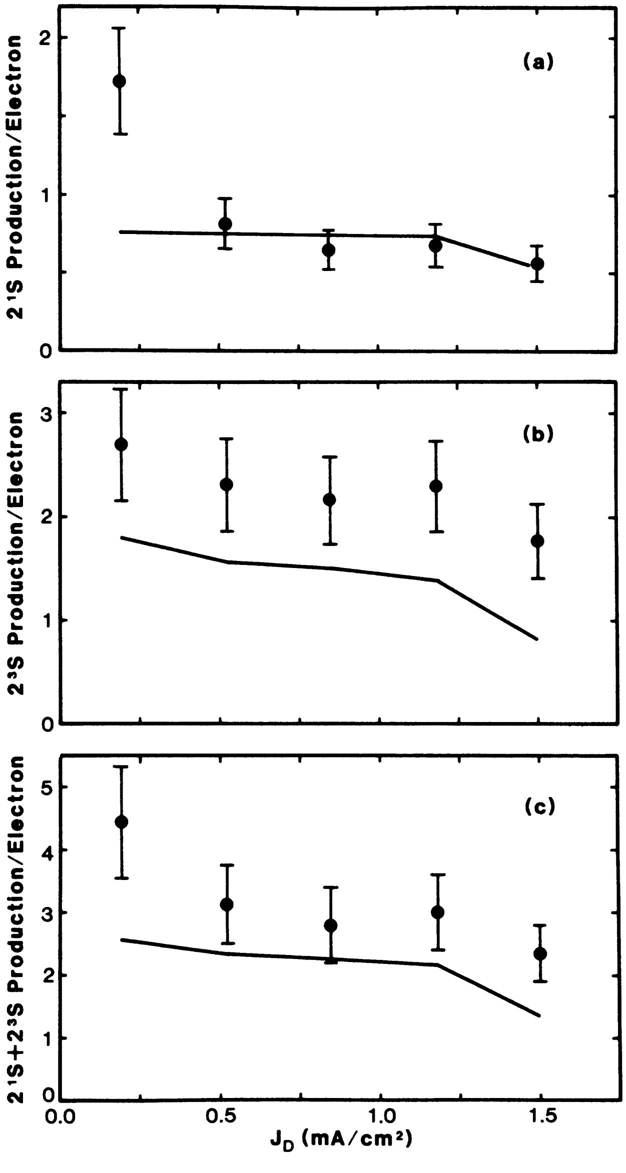

FIG. 13. (a) Helium $2\,^1S$ production, (b) helium $2\,^3S$ production, and (c) total metastable production as a function of discharge current density. The production values presented are spatially integrated production per (net) electron released from the cathode. The points are empirical results with error bars reflecting only the uncertainty of the metastable density measurements. The solid lines are Monte Carlo results using the anisotropic angular distributions for ionizing collision.

The agreement, although imperfect, between simulation and experiment on metastable production provides additional evidence that the current balance of 3.3 is correct. If most of the ions produced in the negative glow drifted to the cathode, then the current balance would be ~ 6. The resulting lower electron current at the cathode would change the analysis of the experimental metastable production per electron. The empirical metastable production per electron would double, and would be in serious discordance with the Monte Carlo simulations.

Figure 13(c) shows typically three metastable atoms produced per net electron emitted from the cathode. This number can be used to estimate the importance of metastable bombardment in electron emission from a cold cathode. If 50% of the metastables diffuse back to the cathode, and if the electron emission coefficient is 0.5, then the metastables could be responsible for 75% of the electron emission from the cathode.[48]

Little and von Engel recognized that neutral particles were playing an important role in emission from a cold cathode.[47] They mention metastables but emphasize uv and vuv photons.[47] Recent measurements indicate that metastables can have electron emission coefficients in excess of 0.5.[48] Photoelectron emission coefficients are rarely as large.

Neutral particles play a major role in electron emission from a cold cathode. It is for this reason that a current balance of 3.3 does not imply an emission coefficient of 0.3 for ion bombardment.

IX. NEGATIVE GLOW

The considerable and detailed experimental and theoretical information on the He discharge described in this work enables us to analyze the negative glow. The negative-glow region starts a distance d_c from the cathode where the cathode-fall field extrapolates to zero. It extends to the anode in our discharge cell. The separation of the electrodes was chosen so that no positive column would form. The negative-glow region is characterized by extremely small electric fields and a high density n_e of low-energy electrons at temperature T_e. These low-energy electrons are *not* described in the Monte Carlo simulations. Results from the Monte Carlo simulations such as $\langle T_{\mathrm{an}} \rangle$, the average energy of electrons striking the anode, are for the high-energy beam electrons. The low-energy electrons are most probably trapped in a potential-energy well. Monte Carlo simulations are not well suited for describing trapped particles.

The analysis of each empirical singlet metastable map as described in Sec. VI produced an effective rate κn_e for metastable spin conversion due to low-energy electrons in the negative glow. This process was discovered by Phelps and the rate constant κ_m was measured for room-temperature ($k_B T_e = 0.025$ eV) electrons.[39] The dependence of this rate constant on electron temperature is $(T_e)^{-1/2}$ because the cross section scales roughly as the inverse of the electron energy.[49] Although we do not *a priori* know the temperature of the low-energy electrons in the negative glow, it is relatively easy to put some limits on it. Surely the temperature of the low-energy electrons must be greater than gas temperature. An upper limit on the electron temperature is determined by noting that the exothermic metastable spin conversion reaction depletes the singlets, but only until the relative singlet versus triplet metastable density comes into thermal equilibrium with the low-energy electron gas. Thus the empirical ratio M_s/M_t in the negative glow must be greater than or equal to

$$\tfrac{1}{3}\exp(-0.79/k_B T_e)\ .$$

These limits on T_e and knowledge of κn_e determine a range of possible electron temperatures and a corresponding electron density for each temperature as given by the expression

$$\begin{aligned}\kappa n_e = n_e[&\kappa_m \sqrt{0.025\ \mathrm{eV}/k_B T_e} \\ &-(M_t/3M_s)\kappa_m \sqrt{0.025\ \mathrm{eV}/k_B T_e} \\ &\times \exp(-0.79\ \mathrm{eV}/k_B T_e)]\ . \end{aligned} \tag{17}$$

This expression is represented by the thick solid lines of Fig. 14. The lower limit for the electron temperature provides a lower limit for the electron density of 2×10^{11} cm^{-3} at intermediate current densities.

Any electron temperature and density consistent with the suppression of the singlet metastables correspond to a short, $\sim 3\times10^{-4}$ cm, Debye length for the negative glow. The Debye length is an electrostatic shielding length for the negative glow. A short Debye length indicates a very abrupt transition between the cathode-fall region and the

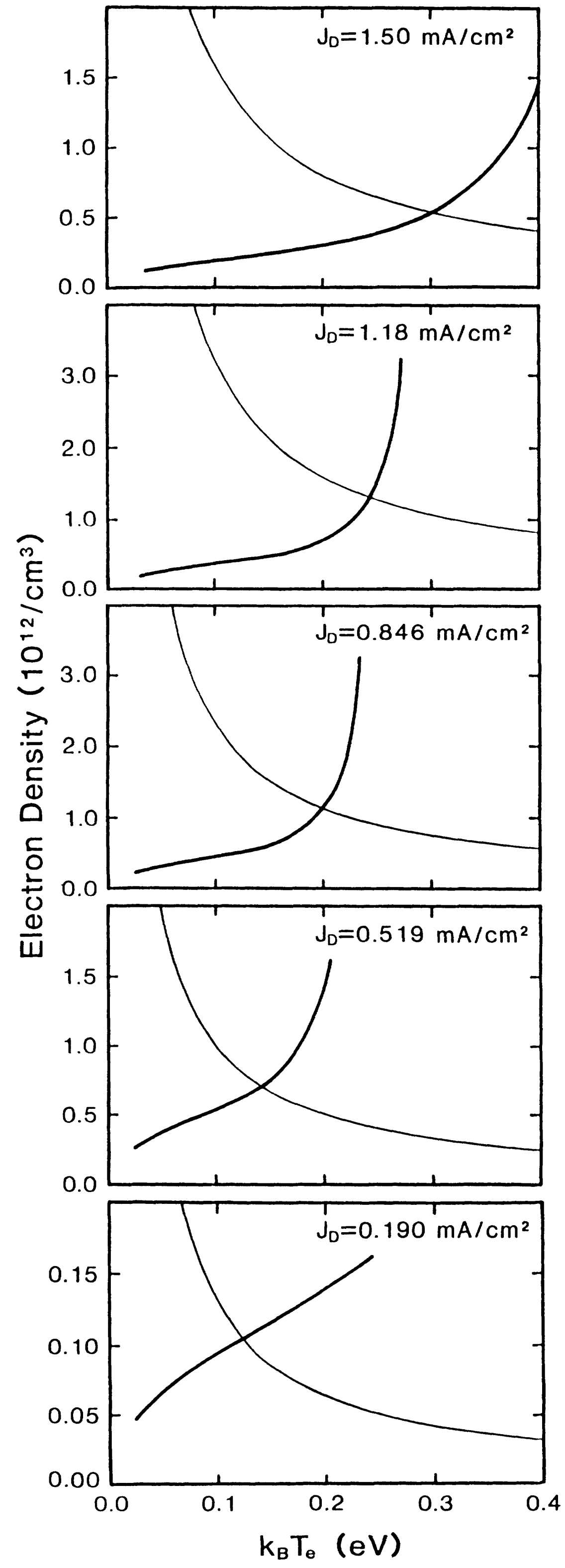

FIG. 14. Negative-glow electron density vs electron temperature for five discharge current densities. The thick line is the relationship from the analysis of the metastable maps. The thin solid line is from the ambipolarlike diffusion of the electron-ion pairs in the negative glow. The intersection of the two lines determines the density and temperature of the low-energy electrons in the negative glow.

negative glow.

The requirement that ion production in the negative glow be balanced by a loss mechanism provides an additional constraint on the low-energy electrons. Two loss mechanisms are possible: recombination or a backdiffusion (drift) of ions to the anode. We do observe He_2 molecular emission bands from the negative glow. These bands are conclusive evidence that some recombination occurs. The recombination rate constant for He is known to be very strongly dependent on the electron temperature.[50] If the electron temperature is near the gas temperature, then recombination could be quite important. Such a low electron temperature in the negative glow seems unlikely.

We suggest that ions in the negative glow drift to the anode in a process analogous to ambipolar diffusion. We note that this mechanism requires a field reversal near the cathode-fall–negative-glow boundary or the point where the cathode field extrapolates to zero. If the field reversal is assumed to be close to the anode then most of the ions produced in the negative glow would drift across the cathode-fall–negative-glow boundary. A large ion current at the boundary causes serious discordances between experiment and simulation in the current balance and the metastable production. The analogy to ambipolar diffusion is not perfect because the electron flux density on the anode must be larger than the ion flux density on the anode by J_D/e. The loss rate of low-energy electrons should be approximately

$$\mu_+ k_B T_e (\pi/2d_{\rm ng})^2/e \ ,$$

where μ_+ is the low-field ion mobility and $d_{\rm ng}$ is the thickness of the negative glow. The factor of $\frac{1}{2}$ is due to the fact that the negative glow is asymmetric; the low-energy electrons cannot diffuse against the cathode field. The rate in the negative glow of ionization per unit volume $\langle P \rangle$ can be determined from the Monte Carlo simulations of Table IV. The rate $\langle P \rangle$ is a spatially averaged quantity

$$\left[\int_{d_c}^{d_c+d_{\rm ng}} P\, dz \right] \Big/ d_{\rm ng} \ .$$

Inclusion of some electron reflection from the anode will increase $\langle P \rangle$, but at most by a factor of 2 and only in the highly abnormal glow discharge at 1.50 mA/cm^2. This model provides a second relation between the density n_e and temperature T_e of the low-energy electrons in the negative glow

$$\langle P \rangle = n_e \mu_+ k_B T_e (\pi/2d_{\rm ng})^2/e \ . \qquad (18)$$

This expression is represented by the thin solid lines of Fig. 14. The intersection of the thin and thick lines determines the density and temperature of the low-energy electrons in the negative glow.

The occurrence of the intersection on the steep portion of the plots of Eq. (17) is an indication that the metastable spin conversion reaction (16a) is proceeding to equilibrium. The relative density of the singlet and triplet metastable is in Boltzmann equilibrium with the low-energy, high-density electrons in the negative glow. Under such conditions the empirical ratio of singlet to triplet metastables is providing the temperature of the negative-glow electrons. The accuracy of this determination of the electron temperature in the negative glow is not easy to assess.

The electron temperature ($k_B T_e \sim 0.25$ eV) is quite reasonable, but the density ($n_e \sim 10^{12}$ cm^{-3}) seems high. The alternate loss mechanism, recombination, could produce a lower electron density but only if the electron temperature is much lower. The suppression of the singlet metastables, which is quite dramatic at intermediate currents, provides a lower limit for the electron density ($n_e \geq 2 \times 10^{11}$ cm^{-3}) and upper limit for the electron temperature ($k_B T_e \leq 0.3$ eV).

X. SUMMARY, CONCLUSIONS, AND FUTURE WORK

Various laser diagnostics are used to study the cathode-fall and negative-glow regions of a He glow discharge. The water-cooled Al cathode is operated over a range of current densities from a near-normal cathode fall of 173 V to a highly abnormal cathode fall of 600 V. Optogalvanic detection of Rydberg atoms is used to map the electric field in the cathode-fall region. The Doppler width of a transition between non-Rydberg levels is used to measure the gas temperature. The gas density is significantly reduced in the abnormal glow discharge due to ion charge exchange heating. Electric field maps and gas density measurements are combined with an analytic treatment of ion transport in the cathode-fall region to determine the current balance or ratio of ion to electron current at the cathode. This current balance is 3.3 and is nearly independent of total discharge current. The densities of He $2\,^1S$ and $2\,^3S$ metastables are mapped using laser-induced fluorescence and laser absorption spectroscopy for absolute calibration. An analysis of the metastable maps provides absolute metastable production rates in the cathode-fall and negative-glow regions and provides a constraint on the density and temperature of the low-energy electrons in the negative glow. The constraint arises from our observation of a suppression of the $2\,^1S$ metastable density in the negative glow. This suppression is due to metastable spin conversion by low-energy electron collisions in the negative glow.

The empirical current balance at the cathode surface and the metastable production rates are compared to theoretical results from Monte Carlo simulations of electron avalanches. A Monte Carlo code, based on the null collision technique for nonuniform fields as developed by Boeuf and Marode, is used to simulate electron avalanches. The agreement between the empirical current balance and the result of Monte Carlo simulations is good. The inclusion of an anisotropic angular distribution for ionizing collisions results in excellent agreement, even in the highly abnormal cathode-fall region where E/N reaches 3000 Td. The agreement between the empirical metastable production rates and the results of Monte Carlo simulations is good.

The high density of low-energy electrons in the negative glow suggests a simple model for the negative glow and suggests the existence of field reversal at the boundary between the cathode-fall and negative-glow regions. The empirical constraint on the density and temperature of the low-energy electrons in the negative glow is combined with an ionization rate predicted by Monte Carlo simulations to determine the density and temperature of the low-energy electrons.

The agreement of the empirical results and results from Monte Carlo simulations lead us to conclude that excitation and ionization, as embodied in the current balance, are quantitatively understood in the cold cathode He discharge. The agreement indicates that the vast majority of ions striking the cathode are produced in the cathode-fall region. The discharge current is carried almost entirely by beam electrons at the cathode-fall negative-glow boundary.

A quantitative microscopic picture of the cathode-fall and negative-glow regions is emerging, but major challenges remain. A major experimental challenge is to measure the relative importance of, and coefficients for, electron emission from the cathode due to ion, metastable atom, and vuv photon bombardment. The measurements should be done *in situ* with a relatively nonperturbing spectroscopic diagnostic. We believe that the spatial and temporal characteristics of carefully chosen optogalvanic effects will provide this information on electron emission. A convincing and fully self-consistent analysis of the optogalvanic effect will likely be difficult. Another experimental challenge is to perform independent measurements of the density and temperature of the low-energy electrons in the negative-glow region. Again, it should be possible to make the measurements with a relatively nonperturbing spectroscopic diagnostic. On the theoretical side there are many challenges. The ultimate goal is to develop relatively simple, efficient models which provide fully self-consistent fields. The models must also have good microscopic detail and absolute accuracy.

ACKNOWLEDGMENTS

This research is supported by the U.S. Army Research Office and the U.S. Air Force Office of Scientific Research under Grant No. AFOSR 84-0328. We thank W. P. Allis for his suggestions and insights, and we thank A. C. Gallagher for his help.

---

[1] P. Segur, M. Yousfi, J. P. Boeuf, E. Marode, A. J. Davies, and J. G. Evans, in *Electrical Breakdown and Discharges in Gases,* Vol. 89A of *NATO Advanced Study Institute, Series B: Physics,* edited by E. E. Kunhardt and L. H. Luessen (Plenum, New York, 1983), p. 331.

[2] W. H. Long, Northrup Research and Technology Center, Technical Report No. AFAPL-TR-79-2038, 1978. (Available as Doc. No. ADA 070 819 from the National Technical Information Service, Springfield, VA 22161.)

[3] J. E. Lawler, D. K. Doughty, E. A. Den Hartog, and S. Salih, in *Radiative Processes in Discharge Plasmas,* Vol. 149 of *NATO Advanced Study Institute, Series B: Physics,* edited by J. M. Proud and L. H. Luessen (Plenum, New York, 1986), p. 525.

[4] M. Ohuchi and T. Kubota, J. Phys. D **16**, 1705 (1983).

[5] P. Bayle, J. Vacquie, and M. Bayle, Phys. Rev. A **34**, 360 (1986); **34**, 372 (1986).

[6] K. G. Emeleus, J. Phys. D **14**, 2179 (1981).

[7] K. Kumar, Phys. Rep. **112**, 319 (1984).

[8] J. Dutton, J. Phys. Chem. Ref. Data **4**, 577 (1975).

[9] T. J. Moratz, L. C. Pitchford, and J. N. Bardsley, J. Appl. Phys. **61**, 2146 (1987).

[10] K. Kitamori, H. Tagashira, and Y. Sakai, J. Phys. D **11**, 283 (1978).

[11] E. J. Lauer, S. S. Yu, and D. M. Cox, Phys. Rev. A **23**, 2250 (1981).

[12] M. A. Folkard and S. C. Haydon, Aust. J. Phys. **24**, 527 (1971).

[13] J. H. Ingold, in *Gaseous Electronics,* edited by M. N. Hirsch and H. J. Oskam (Academic, New York, 1978), Vol. I, p. 24.

[14] K. G. Muller, Z. Phys. **169**, 432 (1962).

[15] L. Friedland, J. Phys. D **7**, 2246 (1974).

[16] D. K. Doughty and J. E. Lawler, Appl. Phys. Lett. **45**, 611 (1984).

[17] J. P. Boeuf and E. Marode, J. Phys. D **15**, 2169 (1982).

[18] C. A. Moore, G. P. Davis, and R. A. Gottscho, Phys. Rev. Lett. **52**, 538 (1984).

[19] D. K. Doughty, S. Salih, and J. E. Lawler, Phys. Lett. **103A**, 41 (1984).

[20] R. Warren, Phys. Rev. **98**, 1650 (1955).

[21] B. N. Ganguly and A. Garscadden, Appl. Phys. Lett. **46**, 540 (1985).

[22] M. L. Zimmerman, M. G. Littman, M. M. Kash, and D. Kleppner, Phys. Rev. A **20**, 2251 (1979).

[23] C. E. Moore, *Atomic Energy Levels,* Natl. Bur. Stand. Ref. Data Ser., Natl. Bur. Stand. (U.S.) Circ. No. 35 (U.S. GPO, Washington, D.C., 1971).

[24] A. R. Edmonds, J. Picart, N. Tran Minh, and R. Pullen, J. Phys. B **12**, 2781 (1979).

[25] D. K. Doughty and J. E. Lawler, Phys. Rev. A **28**, 773 (1983).

[26] D. K. Doughty and J. E. Lawler, Appl. Phys. Lett. **42**, 234 (1983).

[27] T. F. Gallagher, S. A. Edelstein, and R. M. Hill, Phys. Rev. A **15**, 1945 (1977).

[28] W. L. Wiese, M. W. Smith, and B. M. Glennon, *Atomic Transition Probablities,* Natl. Bur. Stand. Ref. Data Ser., Natl. Bur. Stand. (U.S.) Circ. No. 4 (U.S. GPO, Washington, D.C., 1966), Vol. I.

[29] B. N. Ganguly, J. R. Shoemaker, B. L. Preppernau, and A. Garscadden, J. Appl. Phys. **61**, 2778 (1987).

[30] The pressure-broadening coefficient of 42.0±2.7 MHz/Torr at 292 K for the 501.6-nm transition is from J. E. Lawler, Ph.D. thesis, University of Wisconsin, 1978.

[31] J. E. Lawler, Phys. Rev. A **32**, 2977 (1985).

[32] G. H. Wannier, *Statistical Physics* (Wiley, New York, 1966), p. 462.

[33] F. W. J. Olver, in *Handbook of Mathematical Functions,* edited by M. Abramowitz and I. A. Stegun (Dover, New York, 1964), pp. 376 and 416.

[34] M. Abramowitz, in *Handbook of Mathematical Functions,* edited by M. Abramowitz and I. A. Stegun (Dover, New York, 1964), pp. 498 and 501.

[35] G. Arfken, *Mathematical Methods for Physicists* (Academic, New York, 1985), p. 897.

[36]H. Helm, J. Phys. B **10**, 3683 (1977).

[37]S. Sinha, S. L. Lin, and J. N. Bardsley, J. Phys. B **12**, 1613 (1979).

[38]H. F. Wellenstein and W. W. Robertson, J. Chem. Phys. **56**, 1072 (1972); **56**, 1077 (1972).

[39]A. V. Phelps, Phys. Rev. **99**, 1307 (1955).

[40]R. A. Buckingham and A. Dalgarno, Proc. R. Soc. London, Ser. A **213**, 506 (1952).

[41]D. C. Allison, J. C. Browne, and A. Dalgarno, Proc. Phys. Soc. London **89**, 41 (1966).

[42]R. W. LaBahn and J. Callaway, Phys. Rev. A **2**, 366 (1970); Phys. Rev. **180**, 91 (1969); **188**, 520 (1969).

[43]G. D. Alkhazov, Zh. Tekh. Fiz. **40**, 97 (1970) [Sov. Phys.—Tech. Phys. **15**, 66 (1970)].

[44]D. A. Doughty, E. A. Den Hartog, and J. E. Lawler, Phys. Rev. Lett. **58**, 2668 (1987).

[45]A. V. Phelps and L. C. Pitchford, Phys. Rev. A **31**, 2932 (1985).

[46]M. J. Druyvesteyn and F. M. Penning, Rev. Mod. Phys. **12**, 87 (1940).

[47]P. F. Little and A. von Engel, Proc. R. Soc. London, Ser. A **224**, 209 (1954).

[48]R. D. Rundel, F. B. Dunning, J. S. Howard, J. P. Riola, and R. F. Stebbings, Rev. Sci. Instrum. **44**, 60 (1973).

[49]W. C. Fon, K. A. Berrington, P. G. Burke, and A. E. Kingston, J. Phys. B **14**, 2921 (1981).

[50]R. Deloche, P. Monchicourt, M. Cheret, and F. Lambert, Phys. Rev. A **13**, 1140 (1976).